

REPORT DOCUMENTATION PAGE

AFRL-SR-AR-TR-03-

Public reporting burden for this collection of information is estimated to average 1 hour per response, including the time for review, data needed, and completing and reviewing this collection of information. Send comments regarding this burden estimate or any other aspect of this collection of information, including suggestions for reducing the burden, to Washington Headquarters Services, Directorate for Information Operations and Reports (44302). Respondents should be aware that notwithstanding any other provision of law, no person shall be subject to any penalty for failing to provide information unless it is specifically required by law. PLEASE DO NOT RETURN YOUR FORM TO THE ABOVE ADDRESS.

in the
reducing
2202-

1. REPORT DATE (DD-MM-YYYY) 05-03-2003		2. REPORT TYPE FINAL TECHNICAL		3. DATES COVERED (From - To) 12/15/1999 - 11/30/2003	
4. TITLE AND SUBTITLE DNS STUDIES OF TRANSITIONAL HYPERSONIC REACTING FLOWS OVER 3-D HYPERSONIC VEHICLES				5a. CONTRACT NUMBER	
				5b. GRANT NUMBER F49620-00-1-0101	
				5c. PROGRAM ELEMENT NUMBER	
6. AUTHOR(S) XIAOLIN ZHONG				5d. PROJECT NUMBER	
				5e. TASK NUMBER	
				5f. WORK UNIT NUMBER	
7. PERFORMING ORGANIZATION NAME(S) AND ADDRESS(ES) UNIVERSITY OF CALIFORNIA, LOS ANGELES MECHANICAL AND AEROSPACE ENGINEERING DEPARTMENT 420 WESTWOOD PLAZA, 46-147C, ENGINEERING 4 BUILDING LOS ANGELES, CA 90095				8. PERFORMING ORGANIZATION REPORT NUMBER	
9. SPONSORING / MONITORING AGENCY NAME(S) AND ADDRESS(ES) AIR FORCE OFFICE OF SCIENTIFIC RESEARCH AFOSR/NA DIRECTORATE OF AEROSPACE SCIENCE 4015 WILSON BOULEVARD, RM 713 ARLINGTON VA 22203-1954				10. SPONSOR/MONITOR'S ACRONYM(S)	
				11. SPONSOR/MONITOR'S REPORT NUMBER(S)	

12. DISTRIBUTION / AVAILABILITY STATEMENT

APPROVED FOR PUBLIC RELEASE
DISTRIBUTION IS UNLIMITED

13. SUPPLEMENTARY NOTES

20030502 166

14. ABSTRACT

The objectives of this research project are to develop CFD techniques and to conduct DNS studies of fundamental flow physics leading to boundary-layer instability and transition in hypersonic flows. During the three-period, we have conducted extensive DNS studies on the receptivity of a supersonic boundary layer over a blunt cone, and over both sharp and blunt leading edge; and on the receptivity of the Gortler vortices. DNS studies were also compared with Stetson's 1984 stability experiment on Mach 7.99 flow over a blunt cone. Our studies have led to new understanding of a number of hypersonic boundary layer receptivity mechanisms. Such understanding can lead to better tool for the prediction and control of high-speed boundary layer transition.

15. SUBJECT TERMS

HYPERSONIC BOUNDARY LAYERS, RECEPTIVITY, STABILITY, AND TRANSITION, DIRECT NUMERICAL SIMULATION.

16. SECURITY CLASSIFICATION OF:

a. REPORT UNCLASSIFIED	b. ABSTRACT UNCLASSIFIED	c. THIS PAGE UNCLASSIFIED
---------------------------	-----------------------------	------------------------------

17. LIMITATION OF ABSTRACT

UL

18. NUMBER OF PAGES

52

19a. NAME OF RESPONSIBLE PERSON

XIAOLIN ZHONG
19b. TELEPHONE NUMBER (include area code)
(310) 825-2905

FINAL TECHNICAL REPORT

DNS STUDIES OF TRANSITIONAL HYPERSONIC
REACTING FLOWS OVER 3-D HYPERSONIC VEHICLES

(12/15/1999 to 11/30/2002)

Xiaolin Zhong
Professor
Mechanical and Aerospace Engineering Department
University of California, Los Angeles
Los Angeles, California 90095-1597
phone: (310) 825-2905
e-mail: xiaolin@seas.ucla.edu

Prepared for:
Air Force Office of Scientific Research
AFOSR/NA
4015 Wilson Boulevard, Room 713
Arlington VA 22203-1954
Grant Monitor: Dr. John Schmisser/NA
Grant Number: F49620-00-1-0101

March 5, 2003

Contents

1 SUMMARY	3
2 RESEARCH OBJECTIVES	4
3 RESEARCH ACCOMPLISHMENTS	5
3.1 DNS of Receptivity of Stetson's Mach 7.99 Blunt Cone Stability Experiment	5
3.2 DNS Study of Supersonic Boundary-Layer Receptivity Mechanism	7
3.3 Receptivity to Freestream Acoustic Waves for Mach 8 Flow over A Sharp Wedge	8
3.4 Leading Edge Receptivity of Görtler Vortices in a Mach 15 Flow over a Blunt Wedge	8
3.5 DNS of Nonlinear Interaction of Hypersonic Görtler Vortices and Second Mode Waves	9
3.6 DNS of Transient Growth in a Mach 15 Boundary Layer over a Blunt Leading Edge	9
3.7 New Nonuniform-Grid High-Order Schemes and Parallel Implicit Algorithms	10
4 SUMMARY OF RESEARCH ACCOMPLISHMENTS	11
5 RESULTS ON HYPERSONIC BOUNDARY LAYER RECEPTIVITY	12
5.1 Flow Conditions	12
5.2 Steady Base Flow Solutions	14
5.3 LST for Axisymmetric Boundary Layers	16
5.4 Receptivity Results	17
5.5 Results Discussions	27

6 PERSONNEL	28
7 PUBLICATIONS	29
8 ACKNOWLEDGMENT / DISCLAIMER	31
9 REFERENCES	31

1 SUMMARY

The objectives of this research project are to develop CFD techniques and to conduct DNS studies of fundamental flow physics leading to boundary-layer instability and transition in hypersonic flows. During the three-year period, we have conducted extensive DNS studies on the receptivity of a supersonic boundary layer over a blunt cone, and over both sharp and blunt leading edge; and on the receptivity of the Görtler vortices. DNS studies were also compared with Stetson's 1984 stability experiment on Mach 7.99 flow over a blunt cone. Our studies have led to new understanding of a number of hypersonic boundary layer receptivity mechanisms. Such understanding can lead to better tools for the prediction and control of high speed boundary layer transition.

The main research contributions are:

1. It was found that the receptivity mechanisms of hypersonic boundary layers are fundamentally different from those of subsonic boundary layers. The synchronization location between a stable mode I and the second Mack mode plays an important role in the receptivity of the second Mack mode to fast acoustic waves. The synchronization interaction of mode I and the second mode explains the delay of excitation of the second mode in hypersonic flow over a blunt cone.
2. We have studied the receptivity of the transient growth of a hypersonic boundary layer over a blunt wedge. It was found that strong transient growths are obtained in the cases of freestream standing vorticity or entropy waves, but not acoustic waves, and the surface roughness can strongly increase the magnitude of growth.
3. We have conducted DNS studies on the instability and receptivity of Görtler vortices to freestream vorticity waves for the same flow. It was found that the growth of the disturbances near the leading edge is associated with the early transient growth due to the coupling of non-orthogonal eigenvectors.
4. We developed a new high-order nonuniform-grid scheme and a parallel implicit algorithm for DNS of hypersonic flows. High-order schemes are necessary in such flow simulations because lower-order schemes do not have sufficient accuracy to compute small flow details. These new methods and computer codes have been not only applied to our DNS studies, but also extended to other areas of studies, such as MHD control of hypersonic boundary layer stability and transition.

2 RESEARCH OBJECTIVES

The prediction of laminar-turbulent transition in supersonic and hypersonic boundary layers is a critical part of the aerodynamics and heating analyses for the development of hypersonic vehicles. The key for an accurate transition prediction is the understanding of the physical mechanisms that lead to transition. However, many important physical mechanisms leading to hypersonic boundary layer transition are currently still not well understood. Among them, receptivity, which can provide the missing link between environment disturbances and boundary layer instability growth and transition, is currently poorly understood and is the subject of the current investigation. In recent years, direct numerical simulation (DNS) has become a powerful tool in the studies of the stability and transition of supersonic and hypersonic boundary layers.

Supported by AFOSR, we have been developing high-order shock-fitting DNS methods, which can be applied to hypersonic boundary layers over realistic blunt bodies with the effects of nose bluntness, the presence of bow shock waves, and the real-gas effects at high temperatures. In the past several years, we have developed^[1] fifth-order DNS methods and computer codes for the DNS studies of hypersonic boundary layer stability and transition in non-trivial geometries with bow shock effects. We have also studied^[2] the receptivity and stability of a number of 2-D and 3-D hypersonic flows over blunt bodies.

The main objectives of this research are to develop high-order and efficient CFD techniques for DNS of transient hypersonic flows, and to conduct DNS studies of fundamental hypersonic flow phenomena associated with hypersonic (and supersonic) boundary-layer stability and transition in 2-D and 3-D hypersonic flows. The DNS numerical tools, as well as other theoretical approaches such as the linear stability analysis, are used to gain a new fundamental understanding of transition phenomena of 3-D chemically-reacting hypersonic boundary layers. The goal of these studies is to achieve new improvements on the prediction tools for hypersonic boundary layer transition, by incorporating the effects of forcing disturbances.

Four major research tasks have been undertaken in this research project. They are:

- A) DNS of receptivity of Stetson's Mach 7.99 blunt cone stability experiment^[3];
- B) receptivity to freestream acoustic waves for Mach 8 flow over a sharp wedge;
- C) leading edge receptivity of Görtler vortices in a Mach 15 flow over a blunt wedge;
- D) DNS of transient growth in a Mach 15 boundary layer over a blunt leading edge.

The main approach is to use DNS as a research tool to study hypersonic boundary layer receptivity physics. Linear stability analysis (LST) is used in conjunction with DNS to help better understand the flow instability mechanisms in numerical solutions. Our fifth-order upwind finite difference shock fitting method^[4] for the DNS of hypersonic flows with a strong bow shock is used. The use of the high-order shock-fitting scheme makes it possible to obtain highly accurate mean flow and unsteady solutions, which are free of spurious numerical oscillations behind the bow shock.

3 RESEARCH ACCOMPLISHMENTS

The research described in the previous section was carried out in a three-year period from December 15, 1999 to November 30, 2003. The three-year research project supported by this grant has led to the publications of

1. Six papers in the archive journals or book chapters,
2. Thirteen conference papers (mainly AIAA papers),
3. Two Ph.D. theses by two students who have graduated with their Ph.D. degrees.
4. The results of this research have also been applied to the area of MHD flow control, as demonstrated by a AFRL SBIR grant in MHD supersonic boundary layer transition control.

More importantly, the research has produced a large amount of new results, and has led to new understanding of a number of hypersonic boundary layer receptivity mechanisms. The understanding of the receptivity process is the key to improving current hypersonic boundary layer transition prediction methods. In the following sections, the major research accomplishments are summarized, followed by more details discussions of some of our new results in hypersonic boundary layer receptivity.

3.1 DNS of Receptivity of Stetson's Mach 7.99 Blunt Cone Stability Experiment

Publications: [9], [13], [18].

Despite decades of extensive research, the prediction of hypersonic boundary layer laminar-turbulent transition is still based on mostly empirical approaches because many mechanisms

leading to the transition are currently not well understood. Among them, receptivity, which is the process of environmental disturbances initially entering the boundary layers and generating disturbance waves in the boundary layers, can strongly affect the location of transition. Stetson's stability^[3] experiment of Mach 7.99 flow over a 7° blunt cone is one of the few stability experiments that contain detailed instability wave information (see Fig. 1). We conducted a numerical simulation study of the receptivity to freestream fast acoustic disturbance waves for this flow, and compared the numerical results with experimental results and with the numerical simulation results reported by Herbert and Esfahanian^[5].

In hypersonic boundary layer flow involving a blunt nose, the receptivity to freestream disturbances is altered considerably by the presence of bow shock and entropy layer created by the blunt nose. It is crucially important that the interaction of disturbance waves with the bow shock is accurately computed in the numerical simulations of the receptivity. In our studies, both steady and unsteady flow solutions for the receptivity problem are obtained by computing the full Navier-Stokes equations using a fifth-order accurate shock-fitting finite difference scheme, which accurately accounts for the effects of bow-shock/free-stream-sound interactions. In addition, a normal-mode linear stability analysis is used to study the stability and receptivity properties of the boundary layer.

It was found that the receptivity mechanisms of hypersonic boundary layers are fundamentally different from those of subsonic boundary layers. The main new findings are that the second mode waves are not excited in the early region along the cone surface where they are predicted to be unstable by the linear stability analysis. The results show that the delay of the second mode excitation is a result of the fact that the receptivity process is governed by resonant interactions among the forcing waves and a number of boundary layer wave modes. It was found that the synchronization location between a stable mode I and the second mode plays an important role in the receptivity of the second Mack mode to fast acoustic waves. The synchronization interaction of mode I and the second mode explains the delay of excitation of the second mode in current hypersonic flow over a blunt cone.

Figure 2 shows the steady flow solutions. The locations of bow shock obtained by Esfahanian and Herbert^[6] are also marked in the contour plot of the figure. Our current solutions for the shape of the bow shock agree very well with the experimental results and those of Esfahanian and Herbert. This figure also shows that the current solutions of the steady pressure and velocity profiles compare very well with those of Esfahanian and Herbert and reasonably well with the experimental results. Figure 3 shows the unsteady solutions for the development of wave amplitudes of pressure perturbations in the boundary layer. The forcing waves are a group of free-stream planar fast acoustic waves with 15 frequencies. The lines in the first plot represent 15 different frequencies of $f = n f_1^*$, where $f_1^* = 14.922 kHz$. The figure shows the development of wave modes induced by the freestream forcing waves. However, there is no apparent presence of the unsteady second mode in the main computational region until at the end of the computational domain. This was an unexpected result

because the LST analysis has shown that the second mode is unstable starting from the region near $x/r = 90$ for frequency at 149.2 kHz ($n = 10$). This fact is a result of the receptivity through the mode I waves in the boundary layer. In the upstream region, the forcing waves induce mode I waves, which induce the second mode downstream through synchronization interaction with the second Mack mode. At the synchronization point, mode I waves convert to the second-mode waves. Because the synchronization point is located downstream of the branch I neutral stability point of the second mode, there are no noticeable second mode components in the region before the synchronization location even though the second is linearly unstable there.

3.2 DNS Study of Supersonic Boundary-Layer Receptivity Mechanism

Publications: [3], [4], [8], [14], [19].

Understanding the receptivity process is critical for prediction and control of boundary layer transition. Fedorov and Khokhlov^[7] performed a theoretical study on the process. In spite of its simple geometry, receptivity of a supersonic boundary layer over a flat plate has complex wave-mode interactions. We used the 5th-order shock-fitting scheme to study the receptivity mechanisms in a Mach 4.5 boundary layer over a flat plate subject to freestream disturbances. The effects of frequencies, amplitudes and orientation angles of free stream disturbances were investigated. An LST-code based on a multi-domain spectral method has been developed to identify instability modes. The specific flow conditions are the same as Kendall's^[8] experiment of Mach 4.5 flow over a flat plate. Figures 4 shows the results of a test case where a plane acoustic wave with orientation angle $\theta_{ac} = 0$ and a frequency of $F = 2.2 \times 10^{-4}$ enters the bow shock from the freestream. The phase velocities of various wave modes in the boundary layer show that there are two branches of the wave modes near the leading edge, where the phase velocities of the two modes approach $1 + 1/M_\infty$ (fast acoustic mode) and $1 - 1/M_\infty$ (slow acoustic mode). The DNS results show a very complex wave pattern with the co-existence of several boundary layer wave modes excited by the forcing waves. Both the mode-I and the mode-II boundary-layer disturbances are generated due to resonance with the acoustic waves. The mode I can convert to the unsteady second mode after it synchronizes with the second mode. Extensive parametric numerical studies have been carried out to better understand the receptivity of different wave modes by forcing disturbances.

3.3 Receptivity to Freestream Acoustic Waves for Mach 8 Flow over A Sharp Wedge

Publication: [10].

The receptivities to freestream fast and slow acoustic waves for a Mach 8 flow over a sharp wedge are studied. The main objective is to understand the receptivity mechanisms and to compare the receptivity mechanisms between fast and slow acoustic forcing waves. The specific flow is a Mach 8 flow over a sharp wedge with half-angle 5.3° , which was studied by Malik *et al.* [9]. The main finding of this study is that the second-mode receptivity to freestream slow acoustic waves is an order of magnitude stronger than that to the fast acoustic waves due to their different receptivity mechanisms.

Figure 5 shows the results of the two sets of receptivity studies. Before acoustic waves enter the boundary layer, they are first processed by the shock wave. The figure shows different patterns of boundary-layer disturbances are generated for the two cases. There is a boundary-layer mode change located near $x^* = 0.34m$ for those induced by fast acoustic waves, while there is no apparent mode change for the slow acoustic wave cases. In receptivity to freestream fast acoustic waves, as shown in our previous study on receptivity of supersonic boundary-layer flow [10], mode I waves are first generated and amplified due to resonant interactions with the forcing fast acoustic waves, followed by an excitation of the Mack mode in the synchronization region between mode I waves and the first-mode waves. On the other hand, in receptivity to freestream slow acoustic waves, the first Mack mode waves are generated directly through the resonant interactions with the forcing slow acoustic waves near the leading edge. As a result, the receptivity to slow acoustic is an order of magnitude stronger than that to fast acoustic waves. The results also show that the receptivity to slow acoustic waves drops off dramatically when the forcing wave orientation angles increase, while there is no such sharp decrease in the fast acoustic wave cases.

3.4 Leading Edge Receptivity of Görtler Vortices in a Mach 15 Flow over a Blunt Wedge

Publications: [2], [12], [15].

We have studied [11] leading edge receptivity of Görtler vortices in a Mach 15 flow over a blunt wedge with a unit Reynolds number of $1.5 \times 10^5/m$. Forcing disturbances are standing or traveling vorticity waves imposed in the freestream. We first investigated receptivity to freestream vorticity waves with zero frequency and with different spanwise wavenumbers. Figure 6 shows examples of the simulation results. All four cases of standing vorticity waves

show that the disturbances increase near the leading edge and decay before they reach the concave surface region, where the Görtler vortices become unstable. The growth of the disturbances near the leading edge is associated with the early transient growth due to the coupling of non-orthogonal eigenvectors. Tumin and Reshotko^[12] studied such transient growth in compressible boundary layer flow and showed that the optimal disturbances are stationary with zero frequency and a particular spanwise wave number. We have also simulated a case of vorticity waves with frequency ($\omega = 50$). Streamwise distribution of the disturbance amplitude is shown in the figure. Vorticity waves with frequency do not show growing disturbances either near the leading edge or in concave region. The main conclusion of this receptivity study is that the Görtler vortices are mainly induced by freestream standing vortices. The traveling freestream vortices and other types of freestream waves induce very weak Görtler vortices in the boundary layer. The penetration of traveling vorticity waves into the boundary layers is difficult since most disturbances are outside the boundary layers, while standing vorticity waves can excite growing disturbances inside boundary layers near the leading edge which excite the Görtler modes in concave region.

3.5 DNS of Nonlinear Interaction of Hypersonic Görtler Vortices and Second Mode Waves

Publications: [2], [20].

We have investigated the interactions of the strong Görtler vortices with second-mode waves in a Mach 15 flow over a blunt body with a concave surface. Three different amplitudes ($10^{-3}U_\infty$, $10^{-2}U_\infty$, and $4 \times 10^{-2}U_\infty$) of second modes are imposed on $0.2U_\infty$ Görtler vortices in a Mach 15 flow. The 2-D second modes develop three dimensionally due to the interaction with Görtler vortices. Figure 7 shows nonlinear development of Görtler vortices in a Mach 15 flow. The figure also shows instantaneous streamwise velocity disturbance contours of Görtler and second modes inside the boundary layer. When the amplitude of second mode is $10^{-3}U_\infty$, the structure of Görtler vortices does not change which indicates that the interactions are weak. However, as the amplitude increases, the vortices are modulated and exhibit the varicose mode structure as the flow moves downstream.

3.6 DNS of Transient Growth in a Mach 15 Boundary Layer over a Blunt Leading Edge

Publications: [1], [11].

We have conducted DNS studies of the receptivity and the initial transient growth of the

flow disturbances in the stagnation point region. The effects of surface roughness are also simulated. The purpose is to study the complete process of receptivity and transient growth of flow disturbances in the leading edge region. The specific flow conditions are $M_\infty = 15$ and $Re_\infty = 60265.5$. The unsteady viscous flows are computed by imposing continuous plane waves on the steady flow variables at the free stream side of the bow shock. The following three kinds of freestream forcing waves have been considered: fast oblique acoustic waves, entropy waves, and vorticity waves. The main findings are: 1) strong transient growths are obtained in the cases of freestream standing vorticity or entropy waves, but not acoustic waves; 2) the surface roughness can strongly increase the magnitude of growth. Figure 8 shows the 3-D streamwise velocity perturbation contours at spanwise wavenumber $\beta = 0.18$. The figure shows that after freestream streamwise vorticity waves enter the computational domain, one kind of disturbance grows inside the boundary layer near the leading edge and decays further downstream. By changing the values of spanwise wavenumber β , we found the largest growth can be approached at $\beta = 0.18$. To study the surface roughness induced by transient growth inside the hypersonic boundary layer near the leading edge, two kinds of surface roughness have been considered in our computational cases. The first kind of surface roughness is simplified as a wavy wall which is sinusoidal and is superimposed on the shape of surface. The second kind of surface roughness is added by using random roughness. This figure shows that, by adding random roughness on the surface, much stronger growth can be achieved near the leading edge.

3.7 New Nonuniform-Grid High-Order Schemes and Parallel Implicit Algorithms

Publications: [5], [6], [7], [18], [21].

We developed a new high-order nonuniform-grid scheme and a parallel implicit algorithm for DNS of hypersonic flows. High-order schemes are necessary in such flow simulations because lower-order schemes do not have sufficient accuracy to compute small flow details. Currently, most high-order finite-difference schemes are derived on uniformly spaced grid points. The schemes are applied to a nonuniform grid by a coordinate transform from the nonuniform physical domain to a uniform computational domain. The main limiting factor in the application of high-order schemes is the numerical instability of high-order boundary closure schemes^[13]. It is necessary to overcome the instability of boundary closure schemes in order to have wide applications of arbitrarily high-order schemes to practical multi-dimensional flow simulations. We showed that it is possible to use high-order (up to 11th order) explicit and compact finite difference schemes with stable boundary closures for high accurate numerical simulation of incompressible and compressible flows. We proposed a simple and effective way to overcome the instability in arbitrarily high-order finite difference schemes with boundary closure schemes. The new high-order (up to 11-th order) schemes

have been analyzed and tested by computing a linear wave equation with oscillatory boundary conditions, and the DNS of the receptivity and stability of hypersonic boundary layer flows over a 2-D blunt body. It was found the high-order schemes are stable and produce a much higher degree of accuracy than lower order schemes.

Meanwhile, we have also developed a flexible high-order parallelized computer code that includes a parallel Fourier spectral method for the direct simulation of fully 3-D hypersonic boundary layers over a blunt body to freestream acoustic disturbance using Navier-Stokes equations. Divide and conquer methods are chosen to solve the banded matrix parallelly because of their good performance. Two kinds of communication methods, all-to-all broadcast and folded skip-decoupling method are studied by computing the same test case. The programming has been completed. Parallel iterative methods are also considered. The new 3-D parallel hypersonic DNS code has been applied to DNS of the receptivity of 3-D hypersonic boundary layer flows over a parabolic leading edge.

4 SUMMARY OF RESEARCH ACCOMPLISHMENTS

In the report period, we have mainly focused on the DNS studies of receptivity of supersonic and hypersonic boundary layer flows. Our studies have led to a new understanding of a number of hypersonic boundary layer receptivity mechanisms. The main research accomplishments are

1. We have conducted receptivity studies on hypersonic flow over a blunt cone, supersonic and hypersonic flow over 2-D flat plate boundary layer, and hypersonic flow over a sharp wedge. It was found that the receptivity mechanisms of hypersonic boundary layers are fundamentally different from those of subsonic boundary layers. The synchronization location between a stable mode I and the second Mack mode plays an important role in the receptivity of the second Mack mode to fast acoustic waves. The synchronization interaction of mode I and the second mode explains the delay of excitation of the second mode in hypersonic flow over a blunt cone.
2. We have studied the receptivity of the transient growth of a hypersonic boundary layer over a blunt wedge. It was found that strong transient growths are obtained in the cases of freestream standing vorticity or entropy waves, but not acoustic waves, and the surface roughness can strongly increase the magnitude of growth.
3. We have conducted DNS studies on the interactions of the strong Görtler vortices with second-mode waves in a Mach 15 flow over a blunt body with a concave surface, and leading edge receptivity of Görtler vortices in the same flow to freestream vorticity waves. It was found that the growth of the disturbances near the leading edge

is associated with the early transient growth due to the coupling of non-orthogonal eigenvectors. The Görtler vortices are mainly induced by freestream standing vortices. The penetration of traveling vorticity waves into the boundary layers is difficult since most disturbances are outside the boundary layers, while standing vorticity waves can excite growing disturbances inside boundary layers near the leading edge which excite the Görtler modes in concave region.

4. In addition to flow physics studies, we developed a new high-order nonuniform-grid scheme and a parallel implicit algorithm for DNS of hypersonic flows. High-order schemes are necessary in such flow simulations because lower-order schemes do not have sufficient accuracy to compute small flow details. These new methods and computer codes have been not only applied to our DNS studies, but also extended to other areas of studies, such as MHD control of hypersonic boundary layer stability and transition.

5 RESULTS ON HYPERSONIC BOUNDARY LAYER RECEPTIVITY

One of the major accomplishments of the current research project is on revealing the unique features of the receptivity of hypersonic boundary layers, as compared to that of subsonic boundary layers. These results are discussed in more detailed in this section. Details of these results have been published in Publications: [3], [4], [8], [9], [10], [13], [14], [18], [19].

5.1 Flow Conditions

Despite decades of extensive research, the prediction of hypersonic boundary layer laminar-turbulent transition is still based on mostly empirical approaches because many mechanisms leading to the transition are currently not well understood. Among them, the receptivity, which is the process of environmental disturbances initially entering the boundary layers and generating disturbance waves in the boundary layers, can strongly affect the location of transition. We conduct a numerical simulation study of the receptivity to freestream acoustic disturbance waves for Mach 7.99 axisymmetric flow over a 7° half-angle blunt cone. The flow conditions are the same as those of the boundary-layer stability experiments reported by Stetson et al. [3]. The current numerical results are compared with those of the experiments and with the numerical simulation results reported by Herbert and Esfahanian [5].

In hypersonic boundary layer flow involving a blunt nose, the receptivity to freestream disturbances is altered considerably by the presence of bow shock and entropy layer created

by the blunt nose. It is crucially important that the interaction of disturbance waves with the bow shock is accurately computed in the numerical simulations of the receptivity. Both steady and unsteady flow solutions for the receptivity problem are obtained by computing the full Navier-Stokes equations using a fifth-order accurate shock-fitting finite difference scheme, which accurately accounts for the effects of bow-shock/free-stream-sound interactions. In addition, a normal-mode linear stability analysis is used to study the stability and receptivity properties of the boundary layer. It is found that, for the case of receptivity to fast freestream acoustic waves with a blunt nose, the second mode waves are not excited in the early region along the cone surface where the second modes are predicted to be unstable by the linear stability analysis. The results show that the delay of the second mode excitation is a result of the fact that the receptivity process is governed by resonant interactions among the forcing waves and a number of boundary layer wave modes.

The air flow conditions for the test case studied in this paper are the same as Stetson et al.'s^[3] experiments on a blunt cone, i.e.,

$$\begin{aligned} M_\infty &= 7.99, Re_{r_n} = \rho_\infty^* U_\infty^* r_n^* / \mu_\infty^* = 33,449 \\ p_t^* &= 4 \times 10^6 \text{ Pa}, T_t^* = 750 \text{ K} \\ \gamma &= 1.4, Pr = 0.72, R = 286.94 \text{ Nm/kgK} \\ \text{Freestream unit Reynolds number: } Re_\infty^* &= 8.78 \times 10^6 \text{ m}^{-1} \\ \text{Blunt cone half angle: } \theta &= 7^\circ \\ \text{Spherical nose radius: } r_n^* &= 3.81 \times 10^{-3} \text{ m} \\ \text{Sutherland's viscosity law: } T_r &= 288 \text{ K}, T_s = 110.33 \text{ K}, \\ \mu_r &= 0.17894 \times 10^{-4} \text{ kg/ms} \end{aligned}$$

The body surface is assumed to be a non-slip wall with an adiabatic wall for the steady base flow solution. The total length of the cone of the experimental model is $L = 1.016 \text{ m}$. The corresponding Reynolds number at this length is $Re_L = 8.92 \times 10^6$.

In order to reproduce similar flow conditions in the numerical simulations of the receptivity process, it is necessary to introduce initial forcing waves to excite the instability waves in the boundary layer. The forcing waves can originate from the freestream or at the wall by surface roughness or vibrations. For a receptivity simulation, it is necessary to impose forcing disturbances in the freestream. In Stetson et al.'s experiments (Fig. 1), the freestream is dominated by acoustic waves generated by the wind tunnel wall. Since the wave fields in the experiment contain a wide range of second-mode frequencies, we introduce, by surface blowing and suction, disturbances of a number of frequencies near the dominant second mode waves in the simulation. The subsequent receptivity and development of the instability waves at these frequencies and their harmonics due to nonlinear interactions are computed by the numerical simulation.

Specifically, we impose simultaneously 15 independent 2-D planar fast acoustic waves of different frequencies in the freestream. The relative amplitudes of the freestream waves among different frequencies are proportional to the wind tunnel spectra. The receptivity problems are studied numerically by solving the unsteady Navier-Stokes equations using a fifth-order shock fitting scheme described in [1]. Body fitted grids are used in the computations, where the oscillating bow shock is treated as an outer computational boundary. The wave interactions with the shock and the development of disturbance waves in the boundary layer are simultaneously resolved by the simulation.

5.2 Steady Base Flow Solutions

The steady base flow solutions of the Navier-Stokes equations for the axisymmetric Mach 7.99 flow over the blunt cone are obtained first by advancing the solutions to a steady state without forcing waves. Some results for the case of isothermal wall at $T_w^* = 800\text{ K}$ have been presented in a previous paper^[14].

The simulation is carried out by using a multi-zone approach using 35 zones with a total of 4200 by 121 grid points for the axisymmetric flow field from the nose to the 250 nose radius surface station. The corresponding Reynolds number at the 190 nose radius surface station is 8.37×10^6 . The results presented in this paper are those for the case of adiabatic wall only.

For their LST calculations, Esfahanian and Herbert^[5,6] performed highly accurate mean flow calculations of the same flow considered in this paper using the thin-layer Navier-Stokes equations and a fine grid of 1300 by 100 points. The shock was computed by a shock-fitting scheme. They compared some of their mean flow solutions with the available experimental results of Stetson et al. In our studies, we compared our results of the full Navier-Stokes equations with those of Esfahanian and Herbert^[5,6] and the experimental results of Stetson et al. It should be pointed out that the full Navier-Stokes equations are used in the current study, while Esfahanian and Herbert used the thin-layer approximation of the Navier-Stokes equations. Though the differences between the two sets of equations should be very small in the downstream region, it is expected that there may be some noticeable differences in the two results in the region near the stagnation streamline, where the thin-layer approximation used in Esfahanian and Herbert's studies may be less accurate.

Figure 9 shows the Mach number contours of the current steady state solution in the first half of the computational domain. In the simulation, the bow shock shape is not known in advance and is obtained as the solution for the freestream computational boundary. The results show that the Mach numbers immediately behind the bow shock approach a constant value of about 7 behind the shock at downstream locations. The locations of bow shock of

the experimental measurements by Stetson et al. are marked as circular symbols in the same figure. The shapes of the two bow shocks agree very well. The locations of the bow shock obtained by Esfahanian and Herbert are also compared with the current solutions. Though the figure is not presented here due to the length limitation, it is found that the numerical shock shapes of Esfahanian and Herbert agree very well with the current results and with those of Stetson et al.'s experiments. Therefore, the current results on the bow shape are accurately predicted by the high-order shock fitting scheme.

Figure 10 compares the steady pressure distributions along the cone surface between the current numerical solutions, the experimental results of Stetson et al.^[3], and thin-layer Navier-Stokes results obtained by Esfahanian and Herbert. There is a discontinuity in surface curvatures at the junction of the sphere nose and cone afterward. The flow experiences an overexpansion at the junction and goes through a recompression along the cone surface afterward. As a result, there is a slight adverse pressure gradient at downstream surface locations as shown in this figure. The figure shows that the surface pressures predicted by the current calculations compare very well with the experimental results and those of Esfahanian and Herbert. The surface temperature distributions along the cone surface for the current case of adiabatic wall are compared in Fig. 11. The current Navier-Stokes solutions agree very well with those of Esfahanian and Herbert of the thin-layer Navier-Stokes solutions. However, both sets of independently obtained numerical solutions predict higher surface temperatures than the experimental results, which indicate that the cone surface in Stetson et al.'s experiments was not perfectly adiabatic. The actual surface temperatures are about 10 to 20% lower than those of the adiabatic wall. Therefore, it is necessary to study the effects of wall temperatures on the receptivity and stability of the same flows. For the current study, only the case of adiabatic wall is considered. The parametric effects of wall temperatures, as well as other effects, will be studied in future papers.

The tangential velocity profiles across the boundary layer at a surface location of $s = 94$ and 128 are shown in Fig. 12. Again, current Navier-Stokes results are compared with those of Esfahanian and Herbert and the experiments. The experimental measurement could only reach to a certain minimum distance from the wall surface because of the size limit of the experimental probes. The figures show that the current results agree very well with those obtained by Esfahanian and Herbert's calculations. The velocity magnitudes agree well with the experiments in the flow region outside of the boundary layer. The computed velocities inside the boundary layer are slightly larger than the experimental values. The discrepancy between the two sets of numerical simulations and the experiments may be due to the uncertainty in experimental measurements. Similarly, the profiles of current pressure and temperatures at $s = 54$ station are compared with those of Esfahanian and Herbert in Figs. 13 and 14. No experimental results are available for comparison in these figures. Again, current results agree very well with the thin-layer Navier-Stokes solutions obtained by Esfahanian and Herbert.

5.3 LST for Axisymmetric Boundary Layers

The linear stability properties of hypersonic boundary layers over the Stetson et al.'s 7° half-angle blunt cone have previously been studied extensively by several researchers^[5,15-17] by using the normal-mode linear stability theory. However, previous LST studies have been mainly focused on the instability of the unstable first and second Mack mode waves. On the other hand, the other wave modes, which are always stable, have not been studied for axisymmetric hypersonic flow over blunt cones. In a previous receptivity study of Mach 4.5 boundary layer flow^[10], it was shown that a family of other wave modes, which are always stable in a linear stability analysis, play an important role in the receptivity process. They are termed mode I, II, III, etc. in [10]. The stable wave modes are generated by the forcing waves through resonant interactions with the forcing waves. Once they are generated, they can interact with the instability waves downstream also through resonant interactions. In order to understand the receptivity process, it is necessary to understand the characteristics of these stable wave modes, in addition to the Mack modes. The characteristics of these stable wave modes in hypersonic flows with nose bluntness have not been studied. Therefore, we will use the LST approach to study the wave mode properties of mode I, mode II, etc. in addition to those of the first and second Mack modes. In addition, the LST analysis is used to identify and analyze the boundary layer eigenmodes generated by forcing disturbances in the numerical simulations.

A LST computer code based on multi-domain spectral method of Malik^[18] is developed for axisymmetric boundary layer flows. Before we use it to carry out the linear stability computations to identify instability modes in the boundary layer, the LST code is validated and compared with experimental results of Stetson et al. and other published LST results for the Mach 7.99 flow considered in this paper.

Figure 15 compares spatial growth rates for the Mach 7.99 flow over the 7° half-angle blunt cone with adiabatic wall for base flow at surface station $s = 175$. The $T' = 0$ boundary condition for wall temperature perturbations is used in the current study. The experimental results of Stetson et al. and other LST results^[5,15-17] are plotted in the same figure for comparison. The figure shows that our results on the second-mode growth rates ($100kHz < f^* < 170kHz$) associated with an isothermal wall boundary condition compare well with other LST results that use the same wall boundary conditions. The differences between the current LST results and those of other authors are mainly due to different mean flow solutions used by different LST computations. The growth rate for the first mode in the current paper is for two-dimensional disturbances only, while those of Malik et al. are for the most unstable three-dimensional first mode. As a result, the two sets of results do not agree in the first mode region of lower frequencies. As stated early in this paper, the linear stability theory predicts much higher second-mode growth rates than the experiments do. Since the DNS simulations of the current paper involve minimum simplifications in flow

models, the growth rates predicted by the full Navier-Stokes simulation are expected to shed light on the reason for the difference in growth rates predicted by LST and those observed in experiments. Figure 15 also shows that at the surface location of 175 nose radii, the second mode instability range is in the range between 100 kHz and 170 kHz. The first mode unstable frequency range is lower than 100 kHz.

5.4 Receptivity Results

Having obtained the steady solution, the receptivity of Stetson et al.'s Mach 7.99 axisymmetric flow over the blunt cone to freestream acoustic waves is simulated by solving the full Navier-Stokes equations. The forcing waves are free-stream planar fast acoustic waves with 15 frequencies. The unsteady flow solutions are obtained by imposing acoustic disturbances on the steady flow solutions in the freestream before reaching the bow shock. The subsequent interaction of the disturbances with the shock and the receptivity of the boundary layer over the cone surface are computed by using the full Navier-Stokes equations.

In the current test case, the freestream acoustic waves contain 15 frequencies with the lowest frequency of $f_1^* = 14.92 \text{ kHz}$ corresponding to dimensionless frequency of $F_1 = 9.04$, and the highest frequency of $f_{15}^* = 223.8 \text{ kHz}$ corresponding to dimensionless frequency of $F_{15} = 135.5$. The effects of entropy layer and nose bluntness on the receptivity are studied by simulation of the full Navier-Stokes equations. The wave modes are identified and the growth rates and wave spectra are compared with LST analysis and with Stetson et al.'s experiments. The relative wave amplitudes among different frequencies in the freestream are set according to the experimental freestream wave spectra reported by Stetson et al. The phase angles of the freestream forcing waves are chosen randomly. The overall wave amplitude is $\epsilon = 6.2578 \times 10^{-4}$, which is small enough so that the receptivity process is linear, with 15 frequencies ($N = 15$).

The unsteady calculations are carried out until the solutions reach a periodic state in time. Temporal Fourier analysis is carried out on local perturbations of unsteady flow variables after a time periodic state has been reached. The Fourier analysis leads to the amplitude of local disturbances and the local phase angle with respect to the forcing waves in the freestream.

The results presented in this subsection are those for the case of zero temperature perturbation boundary condition, while the steady base flow has an adiabatic wall. The unsteady flow solutions are obtained by imposing freestream disturbances, containing 15 frequencies.

Figures 16 to 20 show the development of amplitudes of pressure perturbations for 15 forcing frequencies on the cone surface as functions of x . The pressure perturbation ampli-

tudes, $|p_n(x, y)|$, are obtained by a temporal FFT. Each line in these figures represents one of the 15 frequencies of $f = n f_1$, where $f_1^* = 14.922 \text{ kHz}$ and $n = 1, 2, \dots, 15$. The relative amplitudes in the freestream of waves for each frequency is set to be proportional to those of the Stetson et al.'s experiments.

These figures show that the receptivity process leads to a complex wave structure for induced disturbance waves at the forcing frequencies. The wave structures are different for different frequencies in different sections of the cone surface. As shown in a later part of this paper, the basic receptivity mechanism in the current hypersonic flow over a blunt cone is the same as that of a hypersonic boundary layer over flat plate, which were studied numerically by Ma and Zhong^[10] and theoretically by Fedorov^[7]. For a given frequency, the characteristics of the induced waves undergo gradually changes from dominantly mode I waves near the nose to mode II waves downstream. The second Mack mode waves can only be induced in the receptivity to fast acoustic waves through resonance interaction with the mode I wave induced by the forcing waves. The forcing acoustic waves do not directly interact with the second Mack mode. The main features of the induced waves shown in these figures are briefly described here.

Figure 16 shows the amplitude development along the cone surface of the first six lower frequency waves, ranging from 14.9 kHz to 84.5 kHz ($n = 1, \dots, 6$). The induced wave growth in the boundary layer at these frequencies are not the Mack modes. Instead, they are the stable mode I waves which are induced directly by the forcing acoustic waves through their resonant interactions. The waves developing near the nose in this figure are dominantly mode I waves^[10]. At low frequencies of n equals to 1 and 2, this figure shows an increase of the pressure disturbances at the wall due to the growth of the mode I waves. As frequency increases, the length of this early region of mode I decreases. In the case of $n = 5$, mode I waves reach a maximum value at $x \approx 117$, and decay afterward. The higher the frequency, the earlier the peaks of mode I waves will be reached. This figure also shows wave modulation for the cases of $n = 3$ and $n = 4$, consisting of components of both mode I waves and the forcing acoustic waves due to their resonant interactions.

Figure 17 shows the amplitude development along the cone surface of the next three frequencies ($n = 7, 8, 9$) ranging from 104.5 kHz to 134.3 kHz. Again, the waves developing near the nose are dominantly mode I waves in the region of $x < 75$. The size of the mode I regions decreases as frequencies increase. The mode I waves decay after reaching their peaks. After the decay of the mode I waves and an extended region of low wave amplitudes, the second Mack mode waves start to grow at a later surface location of $s \approx 180$. The second Mack mode waves do not appear in the early surface locations even though the second mode is linearly unstable there according to the linear stability analysis. For the frequency of $n = 9$, the LST analysis has shown that the second mode is unstable starting from the branch I neutral stability point located at $s = 119$. The delay in the development of the second Mack mode is consistent with Stetson et al.'s stability experiments, which also shows

that the disturbances waves are not dominated by the second mode until they reach the region much downstream at 212 surface station. As shown in later sections, the generation of the second Mack mode waves is determined by the resonant interaction between mode I waves and the second Mack mode, which is not related to the branch I neutral stability of the second mode. Therefore, the receptivity process, not the branch I neutral stability point, determines the generation of the second Mack modes.

Figures 18 to 20 show the amplitude development along the cone surface of the higher frequency waves ($n = 10, \dots, 15$) ranging from 149.2 kHz to 223.8 kHz. At these frequencies, the second mode is either stable at high frequencies or weakly unstable with a very small region of instability at relative low frequencies. For these frequencies, the waves developing near the nose are dominantly mode I waves^[10] in the region of $x < 75$. After the decay of the mode I waves, there are no visible second mode waves components because the second Mack mode is either stable or is very weakly unstable. Instead, the amplitude growth after the decay of mode I waves are dominantly mode II waves induced directly by the forcing acoustic waves through resonant interactions.

Figure 18 also shows a strong wave modulation for the cases of $n = 10$ and $n = 11$ in the region of resonant interaction between the forcing waves and mode II. As a result, the oscillations in wave amplitudes consist of components of both mode II waves and the forcing acoustic waves. At higher frequencies of $n = 12$ to 16, the disturbances in the downstream regions are dominated by mode II waves, which grow due to interactions with the forcing acoustic waves. Since mode II is always stable, they reach a peak and decay afterward.

The development of wave amplitudes along the cone surface of all frequencies can be shown more clearly by the frequency spectra of surface pressure perturbations, as shown in Fig. 21 for a number of surface stations ranging from 1.6 to 270 nose radius. The figure shows the spectrum of mainly three dominant wave modes induced in the boundary layer: mode I, the second Mack mode, and mode II. At early surface stations, the wave modes are mainly mode I waves. At locations further downstream along the cone surface, the frequency of dominant mode I waves decreases, while mode II and second mode appears. The second Mack mode of frequencies around 130 kHz does not appear until the waves reach 200 nose radius. The specific regions of the dominant wave modes are marked in Fig. 22. At surface location of 11 nose radius, all wave modes induced in the boundary layer are mainly mode I waves, which are linearly stable and eventually decay. They are generated and amplified in a local region when they are in resonance with the forcing waves. At a later station of $s = 52$, the waves of lower frequencies are still dominated by mode I waves, but mode II start to develop at higher frequency waves. At the downstream location $s = 174$, the mode I wave region continues to decrease. The second mode starts to develop in the frequency around 150 kHz. There are also mode II waves at higher frequencies. At a further downstream location at $s = 274$, unsteady second Mack mode starts to develop in the frequency around 130 kHz. As the boundary layer becomes thicker at further downstream

locations the dominant frequencies of the second mode decreases. There are also mode I and II waves at lower and higher frequencies, respectively.

The disturbances for a given frequency $n\omega_1$ induced in the boundary layer can be represented by the real part of the temporal FFT results. Figure 23 shows the contours of real part of temperature perturbations in the whole computational flow field for the frequency of $f^* = 119.4kHz$ ($n = 8$). The figures show the development of induced waves at a fixed frequency in the entire flow field, from the nose to 273 nose radius surface station downstream. The interaction of forcing waves with boundary layer waves and the subsequent development of the induced waves can be observed in the figure. In the region of $x < 20$, the figure shows that the forcing waves from the freestream passes through the bow shock and enter the boundary layer to generate mode I waves in the boundary layer. This is the interaction region between the forcing waves and mode I stable waves. In the subsequent region of $20 < x < 60$, mode I gradually becomes less synchronized with the forcing waves. Consequently, it develops and decays along the boundary layer in this region. The disturbance waves in the boundary layer are dominantly weakening mode I waves. In the next region of $60 < x < 200$, the wave modes are a mix of forcing waves and mode I waves. At still further downstream, the second Mach mode at this frequency starts to develop further downstream at $x > 220$ as shown in Fig. 23 because the interaction of mode I and the second Mack mode. The figure shows a rope wave, which is a signature feature of the second mode, at the edge of the boundary layer. After they are generated, the second mode waves grow because they are linearly unstable. Though not shown in these figures, the second mode will peak at its Branch II neutral stability point and decays afterward. At still downstream stations, stable mode II will be generated due to resonance interaction with the forcing acoustic waves. The induced mode II waves will grow and decay downstream of the resonance interaction locations.

The induced wave modes, mode I, mode II, and the Mack mode, in the boundary layers are identified by their stability probability and by their perturbation patterns. Figure 24 shows the contours of real part of temperature perturbations in localized regions of the flow field for three different modes, i.e., mode I in the region around 170 nose radius at $f^* = 119.4kHz$ ($n = 8$), mode II in the region around 261 nose radius at $f^* = 179.1kHz$ ($n = 12$), and the second Mack mode in the region around 261 nose radius at $f^* = 119.4kHz$ ($n = 8$). The figure shows that the wave structures inside the boundary layer are different from these three wave modes. mode I and II have distinctively different structure from the second Mack mode the the region near the wall. The second Mack mode has a typical "rope wave" structure with strong perturbation at the edge of the boundary layer, while mode I and II have stronger wave amplitudes in the boundary layer. The wave structures of mode I are slightly different from those of mode II in the middle region of the boundary layers. The computationally obtained wave modes in the boundary layer will be identified by comparison with the LST results in later sections.

The stability of hypersonic boundary layer flow over the Stetson et al.'s 7° half-angle blunt cone has been studied extensively^[5,15-17] by using the normal-mode linear stability theory. These previous LST studies mainly focused on the growth rates of the most unstable first and second Mack mode waves. In Ma and Zhong's receptivity study of Mach 4.5 boundary layer flow^[10], it was found that a family of other wave modes, which are stable in a linear stability analysis, play an important role in the receptivity process. They were termed mode I, II, III, etc. in [10]. These stable wave modes, which are generated by the forcing waves through resonant interactions, can interact with the instability waves once they are generated. In order to understand the receptivity process, it is necessary to understand the characteristics of these stable wave modes in the current axisymmetric flow in addition to the Mack modes. So far, the characteristics of these stable wave modes in hypersonic flows with nose bluntness have not been studied. Therefore, in this section, the LST approach is first used to study the wave mode properties of mode I, mode II, etc. besides the first and second Mack modes. Subsequently, the results of the LST analysis are used to identify and analyze the boundary layer eigenmodes generated by forcing disturbances in the numerical simulations.

A similar LST study is carried out in the current study for axisymmetric Mach 7.99 boundary-layer flow over the 7° half-angle blunt cone. Figure 25 shows the distributions of the phase velocities of three discrete modes, i.e., mode I, mode II and the Mack modes, changing as functions of the frequencies at a fixed surface station of $s = 175$. The phase velocities of the fast acoustic wave ($1 + 1/M_\infty$), entropy/vorticity wave (1), and slow acoustic wave ($1 - 1/M_\infty$) are also shown in the figure for comparison. Both mode I and mode II originate with an initial phase velocity of the fast acoustic wave ($1 + 1/M_\infty$). Before these two modes become distinct modes, their eigenvalues merge with the continuous spectra at the same velocity as the fast acoustic waves. After these two wave modes appear as discrete modes, their phase velocities decrease gradually with increasing ω . As a result, the differences of the phase velocities between mode I and mode II and that of the fast acoustic waves become larger as ω becomes larger.

Figure 25 also shows that the distributions of phase velocities vs ω for both mode I and mode II are discontinuous when they cross the line of the phase velocity of the entropy/vorticity wave (1). This discontinuity of the phase velocity curves is a result of the fact that the trajectory of mode I passes across middle continuous spectra. In fact, mode I merges with this continuous spectra when it intersects the middle continuous spectra. Later, another eigenvalue from this continuous spectra becomes discrete mode I. Therefore, there is a gap in the phase velocity curve of mode I shown in Fig. 25. Consequently, there are two branches of mode I (and mode II) in the phase velocity curves. They are labeled as mode I (1) and mode I (2), respectively. With the further increase of ω , the phase velocities of mode I continue to decrease further and intersect with the phase velocity curve of the Mack modes. At the intersection point ($\omega = 0.1825$), mode I is synchronized with the second Mack mode because the two modes have the same frequency and phase velocity there. In addition, both modes have very similar profiles of perturbation eigenfunctions. The only exception is that

the two modes have different growth rates at this synchronization location.

The phase velocity curve for mode II shown in Fig. 25 is very similar to that of mode I. Specifically, a discrete mode II appears from the continuum spectra related to the fast acoustic waves, and its phase velocities decrease as ω increases. The curve also becomes discontinuous when it crosses the line corresponding to the entropy/vorticity wave. Mode II will eventually intersect with the Mack mode at a high frequency. This intersection point is also a synchronization location for the two modes.

The phase velocities for Mack modes, on the other hand, show an opposite trend as ω increases. For very small ω , Fig. 25 shows that the Mack modes are synchronized with the slow acoustic waves. As ω increases, the phase velocities of the Mack modes increase. They will interact with mode I and later mode II as ω increases further. The locations of the intersection points between the Mack mode curve and the curves of mode I and mode II are the wave synchronization locations. Through the resonant interactions at these synchronization locations, the Mack modes interact directly with mode I and mode II. The figure shows that the fast acoustic waves do not interact directly with the Mack modes.

At the synchronization location between mode I and the Mack modes, two kinds of modes have the same frequency and wave speed (or real part of the wave number, α_r). But they are distinctive by the fact that they have very different growth rates, or the imaginary part of the wave number, α_i . The growth rates (α_i) of different normal modes, at the same flow conditions as those of Fig. 25, are plotted in Fig. 26. While the growth rates of Mack modes are continuous, there are two gaps in the growth rate curves for mode I and mode II. It shows that both mode I and mode II are modes that are always stable. When they initially appear at relatively low frequency, these two modes are close to zero growth rates. As ω increases, their growth rates are always on the stable side and become more and more stable.

On the other hand, the growth rates of the Mack modes are represented by a single continuous curve in Fig. 26. The figure shows that the Mack modes are unstable in multiple regions of different frequencies. Mack modes are slightly unstable in the range of ω between 0.0485 and 0.117. The Mack mode in this range is the conventional first mode identified by Mack^[19]. Though not shown here, the first Mack mode is most unstable when the waves are three-dimensional oblique waves. On the other hand, in the range of ω between 0.171 and 0.243, the unstable Mack modes are the conventional second mode. In this range, the growth rates of the second mode increase dramatically to a peak and decay afterward. As shown in Fig. 25 and 26, the first mode and the second mode identified by Mack are in fact different sections of a single wave mode. Therefore, in this paper, both the first and the second Mack mode are simply called Mack modes for convenience of discussion.

Figure 15 compares spatial growth rates at surface station $s = 175$ for the Mack modes at a range of frequencies. The experimental results of Stetson et al. and other LST results

are plotted in the same figure for comparison. The figure shows that our LST results for the second Mack mode growth rates compare reasonably well with other LST results that use the same wall boundary conditions. The small differences among the LST results obtained by different authors are mainly due to different mean flow solutions used by different LST computations. These LST results predict that, at 175 surface station, the second Mack mode is unstable in an approximate frequency range between 100 kHz and 170 kHz. The second Mack mode of 130 kHz has the largest growth rate at this surface station. The first mode unstable frequency range is lower than 100 kHz. The experimental frequency of the second Mack mode with the maximum growth rates is approximately 140 kHz, which is about 7.7% larger than that predicted by LST. On the other hand, compared with Stetson's experimental results, the linear stability theory predicts much higher growth rates than the experiments do.

Another important characteristic of boundary-layer instability is the neutral stability curve, which is the trajectory of neutral stability locations of the Mack modes. Figure 27 compares the present neutral curve of the Mack modes with that of obtained by Malik^[15]. There are two peaks in the curve. The first peak with lower frequencies (lower than 100 kHz) is for the first Mack mode, while the second peak with higher frequencies (higher than 100 kHz) is for the second Mack mode. In the figure, R is the Reynolds number based on boundary layer thickness length scale. The value of R in the figure can be converted into non-dimensional surface length s by

$$s = R^2 / Re_{r_n} \quad (1)$$

where Re_{r_n} is the freestream Reynolds number based on nose radius. For the current flow, $Re_{r_n} = 33,449$. The figure shows that overall, there is a good agreement between the present result and Malik's result in the neutral stability curve. There are slight differences between the two sets of results, especially in the boundary region between the first and second Mack modes. The current steady base flow solution is obtained with a much higher grid resolution than that used in Malik's LST calculations. The difference between them is due to different mean flows used in LST analyses. Based on the current result, the critical local Reynolds number (R) for boundary-layer instability is the second mode at surface location of 1580, which corresponds to $s = 75$ and $x = 72.5$. This critical value is very close to Malik's result $R = 1540$ for $s = 70.9$ and $x = 68.8$. Below this critical Reynolds number, all boundary-layer modes are stable. As for the first Mack mode, the first unstable two-dimensional first mode appear at $R = 2270$, which corresponds to $s = 154$ surface station. Figure 27 also shows that both the first mode and the second mode are stable for high frequencies above $f^* = 180 \text{ kHz}$.

The results of the linear stability theory are used to identify different dominant wave modes in the boundary layer induced by freestream fast acoustic waves. Phase velocities and structures of boundary-layer disturbances from the unsteady flow numerical simulations are compared with the corresponding values from eigenvalues and eigenfunctions of the linear stability theory at the same frequency. In the numerical simulations, receptivity results of

15 independent frequencies are obtained. In this paper, only the results of three typical frequencies are chosen for the comparisons with the LST results. These three frequencies are 74.61 kHz for $n = 5$, 119.4 kHz for $n = 8$, and 223.8 kHz for $n = 15$. The evolution of pressure perturbation amplitudes ($|p_n(x, y)|$ for $n = 5, 8, 15$) on the wall due to freestream disturbances at these three frequencies are redrawn in Fig. 28. The figure shows the growth and decay of wave amplitudes along the surface for each frequencies. The induced waves at these three frequencies are dominated by different modes in different regions. These modes include the Mack modes, mode I, and mode II. For the case of $n = 5$ frequency, the induced waves in the boundary layer are mainly mode I waves. For the case of $n = 8$ frequency, on the other hand, the induced waves in the boundary layer are mainly mode I waves before 65 nose radius surface station, and the second Mack mode after 230 nose radius station. Finally, for the case of $n = 15$ frequency, the induced waves in the boundary layer are mainly mode II waves. For the receptivity to freestream acoustic waves, no significant first Mack mode components are found in the boundary layer, despite the fact that the first mode is also linearly unstable in the present boundary layer as shown by Fig. 27. In order to identify the wave modes in different regions at each frequency, the phase velocities of different wave modes are tracked from upstream to downstream by the linear stability theory. The wave structures of mode I at $n = 5$, the second Mack mode at $n = 8$ and mode II at $n = 15$ from numerical simulations are compared with those from the linear stability theory at their respective locations.

The phase velocities of the induced boundary-layer disturbances obtained from the numerical simulations are calculated based on pressure perturbations on the wall surface by using the temporal Fourier analysis. The value corresponds to streamwise wave number (α_r) of a single wave if the numerical solutions are dominated by a single discrete wave mode in a local region. On the other hand, if the numerical solutions contain a mixture of two or more wave modes, the values of streamwise wave numbers calculated will demonstrate the result of modulation of these mixed wave modes. At each frequency, the induced boundary-layer disturbances can be identified by comparing the wave numbers, the phase velocities, and wave structures from simulations with the eigenvalues and eigenfunctions obtained from the LST calculations. Here, the three typical frequencies with $n = 5, 8$ and 15 are chosen for the comparison of both eigenvalues and eigenfunctions. For other frequencies, the results of the comparison between the numerical simulations and LST are very similar to those of these three typical frequencies.

The development of wave components with a higher frequency of 119.4 kHz is considered next. At this frequency, Fig. 27 shows that the Branch I neutral stability point, which marks the starting point where the unstable region of the Mack modes, is located at the surface station of 143.4 nose radius. The unstable Mack mode at this frequency is the second mode. As shown in Fig. 28, at this frequency, the amplitudes of the induced disturbances in the boundary layer increase initially, reach a peak approximately at the surface station of 30 nose radius, and decay afterward. In the following region between surface station of 65 nose

radius to 200 nose radius, the amplitudes of the disturbance waves stay at a constant level with slight fluctuations. There is no apparent second Mack mode growth in the second mode unstable region ($x > 143.4$). Eventually, the wave amplitudes increase dramatically in the region after 200 surface station. This significant amplitude growth is a result of the second mode excitation and instability. Similar to the case of $n = 8$ frequency, the wave behavior of the numerical simulation results can be understood by the comparison with the LST results at the same frequency.

Among different frequencies, Fig. 28 shows that the induced boundary-layer disturbances are most strongly amplified at frequency of $n = 8$ ($f^* = 119.4 kHz$) near the exit of the computational domain. LST is used to identify the dominant normal mode included in boundary-layer disturbances at different locations. At first, the distribution of streamwise wave number and phase velocity of induced boundary-layer disturbances at this frequency is compared with those of LST for different normal modes, which is presented in Figs. 29 and 30. Similar to the results shown in Fig. 25, there is a gap in the streamwise wave number and phase velocity curves of mode I waves according to the LST. The synchronization point between mode I and the Mack modes is located at the surface station of 192 nose radius, which is downstream of the Branch I neutral stability point of the second mode at 143.4 nose radius.

The phase velocities of the numerical solutions of the induced waves in the boundary layer are compared with those of mode I and the second Mack mode. Figure 29 shows that the streamwise wave numbers of the induced waves are very close to those of mode I waves in the early region of $x < 66$, which indicates that the induced boundary-layer disturbances are dominated by mode I waves in this region. These mode I waves are generated by their resonant interactions with the forcing fast acoustic waves near the nose. The induced mode I waves in this region can be confirmed by comparing the wave structures of the numerical simulations with the eigenfunctions of mode I waves obtained from LST. It is found that the induced waves modes in the receptivity simulations agree very well with those of mode I.

Ma and Zhong^[10] showed that the development of mode I waves can be characterized by a non-dimensional frequency ω , which is related to F and R . This observation also applies to the current receptivity of axisymmetric Mach 7.99 flow over a blunt cone. For the two frequencies of $n = 5$ and $n = 8$ discussed so far, the locations of mode I waves reaching a peak amplitudes are $x = 37.1$ for $n = 8$ and $x = 109.2$ for $n = 5$. The corresponding values of the nondimensional frequencies ω can be calculated as: $\omega = 0.083$ ($x = 37.1$) at frequency with $n = 8$, and $\omega = 0.087$ ($x = 109.2$) at frequency with $n = 5$. These two numbers are very close, which also demonstrate that the waves in these two frequencies are indeed mode I waves. This also indicates the similarity in wave patterns of the growth and decay of mode I waves at different frequencies when the distributions are scaled by ω . Again, for the current frequency of $n = 8$, the resonant interaction between mode I waves inside the boundary layer and fast acoustic waves outside the boundary layer results in the amplification of the

induced boundary-layer disturbances in the region with $x < 37.1$.

Meanwhile, the modulation between the mode I waves and the fast acoustic waves, and the stable properties of mode I waves can explain the growth and decay of boundary-layer disturbances during their propagation downstream in the region between $37.1 < x < 190$ (Fig. 28). The wave modulation also leads to strong fluctuations in the distribution of amplitudes of the boundary-layer disturbances in the same region as shown in Figs. 29 and 30. At the earlier surface stations ($x < 66$), this kind of amplitude fluctuations is around the streamwise wave numbers of mode I, when the components of mode I waves included in boundary-layer disturbances are relatively strong. In the subsequent region ($x > 66$), the modulation of wave modes is around the phase velocity of the fast acoustic waves, which indicates the relative dominance of fast acoustic waves included in boundary-layer disturbances in this region. In the region downstream after $x > 200$, the boundary-layer disturbances at frequency with $n = 8$ are strongly amplified as shown in Fig. 28. From distribution of streamwise wave number and phase velocity curves shown in Figs. 29 and 30, the wave numbers and phase velocities of the induced boundary-layer disturbances match those of the second Mack modes in the region after $x > 250$, which shows that Mack mode waves are dominant there.

The identification of induced Mack-mode waves is confirmed by comparing the disturbance structures of the numerical simulations with the eigenfunctions of the second Mack mode from the LST at the station with $x = 271$. Figs. 31 and 32 shows the comparisons of the eigenfunctions for the pressure perturbations and the temperature perturbations, respectively. There is a good agreement in wave structures between the numerical simulation results and those from LST for the second Mack mode. The slight differences in the comparison is because there are other wave components, such as fast acoustic waves, included in the boundary-layer disturbances besides the second-mode waves from the numerical simulation.

Having identified the second Mack-mode waves to be the dominant waves inside the boundary layer the surface region downstream of 200 nose radius, it is not difficult to understand the strong amplification of induced boundary-disturbances because of the instability of the second mode waves after they are generated by the resonant interaction with mode I. The growth rates of boundary-layer normal modes at frequency at $n = 8$ from the LST are shown in Fig. 33. At this frequency, the second-mode Branch I neutral stability point is located at $x = 143.4$. The second Mack-mode waves become unstable in the region of $x > 143.4$. In addition, the growth rates of the second-mode waves reach peak value of $\alpha_i = -0.0051$ at $x = 234$. In other words, the second mode is most unstable and should be strongly amplified at this location. However, there are no amplified second-mode waves at frequency with $n = 8$ shown in Fig. 28 between $143.4 < x < 192$. On the contrary, the amplitude of boundary-layer disturbances slightly decays in this region. Therefore, the generation of the second-mode waves do not coincide with their Branch I neutral stability point. As shown in Figs. 29 and 30, there is much difference in wave number curves between Mack-mode waves

and fast acoustic waves. Thus, there is no direct interaction between Mack-mode waves and the forcing fast acoustic waves. Instead, there is a bridge, i.e., mode I waves, between Mack modes and fast acoustic waves. During propagation downstream, mode I waves generated by fast acoustic waves reach the synchronization point between mode I waves and Mack-mode waves located at $x = 192, \omega = 0.185$. Here, the location of synchronization point in term of ω is very close to that shown in Fig. 25 with $\omega = 0.1825$ at the station $s = 175$ (or $x = 172$) where local Reynolds number R is fixed while frequency is changing. At the synchronization point, both mode I and Mack mode have very similar profiles of eigenfunctions. As a result, mode I waves convert to Mack-mode waves because Mack-mode waves are much more unstable than mode I waves as predicted by the LST calculations, which are shown in Fig. 33. Because the second Mack-mode waves are generated by mode I waves at the synchronization point, there is no amplification of second-mode waves in the region before this point, even though the second Mack mode unstable region begins much earlier. After the generation of the second-mode waves, the boundary-layer disturbances are significantly amplified resulting from the unstable property of the second mode in the downstream region with $x > 192$, which is obviously shown in Fig. 28.

Therefore, it is clear that the strong growth of the disturbance waves in the boundary layer in the region downstream after $x > 200$ is the result of excitation and unstable growth of the second Mack mode. The second mode is generated by its resonant interactions between the mode I waves, which in turn are generated by the forcing fast acoustic waves in the nose region. Such receptivity mechanisms based on resonant interaction between the forcing waves and various boundary wave modes are very different from those the subsonic boundary layers. The resonant interaction mechanisms also explain the fact that the second Mack mode is not generated in the boundary layer before the synchronization point between mode I and the second ($x = 192$), even though the second Mack mode becomes unstable at earlier surface stations at 143.4 nose radius. These receptivity results also demonstrate the importance of the receptivity studies in transition prediction because the initial wave generation determines the amplitudes of the subsequent growth of an instability wave.

5.5 Results Discussions

To summarize the general features of the waves induced in the boundary layers, there is a complex development of wave modes induced by freestream acoustic waves. The second mode does not develop in the region where LST predicts unstable second modes to be dominant. The second modes are excited at a later location than predicted by the LST analysis. This delay is shown to be caused by the current receptivity process, and is governed by the resonant interactions between the forcing waves and the stable boundary layer wave modes. There is also a strong presense of the stable boundary layer modes, mode I and mode II in the boundary layers. Mode I is generated in the early region of the flow field near the nose,

while mode II is generated downstream of the second Mack instability region. In order to quantitatively study the induced waves in the boundary layer, it is necessary to identify, by using LST results, the wave modes in the boundary layer in the receptivity process and to identify the cause of the delay in the development of the second mode waves.

It is clear that the synchronization location between mode I and the second mode plays the most important role in the receptivity of the second Mack mode in the boundary layer. In the current flow over a blunt cone, the synchronization location is located downstream of the branch I neutral stability location of the second mode. As a result, there are no noticeable second mode components in the region before the synchronization location even though the second mode is linearly unstable there. In addition, due to the resonant interaction with the forcing acoustic waves, there is amplification of mode I waves in the region upstream and amplification of mode II wave in the region downstream for different frequencies where all normal mode may be predicted to be stable. The delay in the excitation of the second mode in the current receptivity process leads to a delay of the second mode excitation in hypersonic boundary layers over a blunt cone. The results also show that excitation of the mode II waves for higher frequency waves at downstream locations. Overall, the receptivity mechanisms are very different from those of the incompressible boundary layer flow. The resonant interaction between the forcing waves and boundary layer wave modes and the resonant interactions among these normal modes is the main cause of the excitation of the unstable Mack modes in hypersonic boundary layer over a blunt cone.

6 PERSONNEL

The following personnel conducted research for the grant and were partially supported by the grant:

1. Professor Xiaolin Zhong, principal investigator.
2. Chong W. Whang, a Ph.D. student. He graduated with a Ph.D. degree in January 2003.
3. Yanbao Ma, a Ph.D. student.
4. Haibo Dong, a Ph.D. student. He graduated with a Ph.D. degree in January 2003.

7 PUBLICATIONS

The following publications were completed from work supported by this grant:

Ph.D. Theses:

- 1 H. Dong "Parallel Implicit Algorithms for Direct Numerical Simulations of Hypersonic Boundary Layer Stability and Transition," Ph.D. Thesis, Aerospace Engineering, UCLA, 2003.
- 2 C. W. Chong "Numerical Studies on Receptivity and Transition of Gortler Instability in Hypersonic Boundary Layers," Ph.D. Thesis, Mechanical Engineering, UCLA, 2003.

In Journals or Books:

- 3 Y. Ma and X. Zhong "Receptivity of a supersonic boundary layer over a flat plate. Part 1: wave structures and interactions," Accepted for publications by the **Journal of Fluid Mechanics**, 2003.
- 4 Y. Ma and X. Zhong "Receptivity of a supersonic boundary layer over a flat plate. Part 2: receptivity to freestream sound," Accepted for publications by the **Journal of Fluid Mechanics**, 2003.
- 5 H. Dong and X. Zhong, "High-Order Semi-Implicit Schemes for Unsteady Compressible Flow Simulations," **AIAA Journal**, Vol. 40, pp. 869-878, May 2002.
- 6 X. Zhong, C. W. Whang, and Y. Ma "Numerical Simulation of Hypersonic Boundary Layer Stability and Receptivity," **Frontiers of Computational Fluid Dynamics 2002**, edited by D.A. Caughey and M.M. Hafez, World Scientific, New Jersey, pp. 381-396, 2002.
- 7 X. Zhong, "DNS of Hypersonic Boundary Layer Stability and Transition Using High-Order Nonuniform-grid Schemes," **DNS/LES Progress and Challenges**, edited by C. Liu, L. Sakell, and T. Beutner, Greyden Press, Ohio, pp. 195-206, 2001.
- 8 X. Zhong, "Leading-Edge Receptivity to Free Stream Disturbance Waves for Hypersonic Flow Over A Parabola," **Journal of Fluid Mechanics**, Vol. 441, pp. 315-367, 2001.

In Conference Proceedings:

- 9 X. Zhong and Y. Ma, "Numerical Simulation of Leading Edge Receptivity of Stetson's Mach 8 Blunt Cone Stability Experiments," **AIAA paper 2003-1133**, January 2003.
- 10 Y. Ma and X. Zhong, "Receptivity of Freestream Disturbances of Mach 8 Flow over a Sharp Wedge," **AIAA paper 2003-0788**, January 2003.
- 11 H. Dong and X. Zhong, "Numerical Simulations of Transient Growth in a Mach 15 Boundary Layer over a Blunt Leading Edge," **AIAA paper 2003-1226**, January 2003.
- 12 C. W. Whang and X. Zhong, "Leading Edge Receptivity of Görtler Vortices in a Mach 15 Flow over a Blunt Wedge," **AIAA paper 2003-0790**, January 2003.
- 13 X. Zhong and Y. Ma, "Receptivity and Linear Stability of Stetson's Mach 8 Blunt Cone Stability Experiments," **AIAA paper 2002-2849**, June 2002.
- 14 Y. Ma and X. Zhong, "Receptivity to Freestream Disturbances of Mach 4.5 Flow over A Flat Plate," **AIAA paper 2002-0140**, January 2002.
- 15 C. W. Whang and X. Zhong, "Receptivity of Gortler Vortices in Hypersonic Boundary Layers," **AIAA paper 2002-0151**, January 2002.
- 16 H. Dong and X. Zhong, "Time-accurate Simulations of Hypersonic Boundary Layer Stability and Transition over Blunt Bodies Using Implicit Parallel Algorithms," **AIAA paper 2002-0156**, January 2002.
- 17 X. Zhong, "DNS of Hypersonic Boundary Layer Stability and Transition Using High-Order Nonuniform-Grid Schemes," **Invited Paper** in the Third AFOSR International Conference on DNS/LES, University of Texas at Arlington, Texas, August 2001.
- 18 X. Zhong and M. Tatineni, "Stable High-Order Schemes and DNS of Boundary-Layer Stability on a Blunt Cone at Mach 8," **AIAA paper 2001-0437**, January 2001.
- 19 Y. Ma and X. Zhong, "Numerical Simulation of Receptivity and Stability of Nonequilibrium Reacting Hypersonic Boundary Layers," **AIAA paper 2001-0892**, January 2001.
- 20 C. W. Whang and X. Zhong, "Secondary Görtler Instability in Hypersonic Boundary Layers," **AIAA paper 2001-0273**, January 2001.

- 21 H. Dong and X. Zhong, "Implicit Parallel Algorithms for Time-Accurate Simulations of Hypersonic Boundary Layer Receptivity Over Blunt Bodies," *AIAA paper 2001-0438*, January 2001.

8 ACKNOWLEDGMENT / DISCLAIMER

This work was sponsored by the Air Force Office of Scientific Research, USAF, under AFOSR Grant #F49620-00-1-0101. The program manager is Dr. John Schmisser. The views and conclusions contained herein are those of the author and should not be interpreted as necessarily representing the official policies or endorsements either expressed or implied, of the Air Force Office of Scientific Research or the U.S. Government.

9 REFERENCES

References

- [1] Zhong, X., "High-Order Finite-Difference Schemes for Numerical Simulation of Hypersonic Boundary-Layer Transition," *Journal of Computational Physics*, Vol. 144, August 1998, pp. 662-709.
- [2] Zhong, X., "Direct Numerical Simulation of Hypersonic Boundary-Layer Transition Over Blunt Leading Edges, Part II: Receptivity to Sound (Invited)," *AIAA paper 97-0756*, January 1997.
- [3] Stetson, K. F., Thompson, E. R., Donaldson, J. C., and Siler, L. G., "Laminar Boundary Layer Stability Experiments on a Cone at Mach 8, Part 2: Blunt Cone," *AIAA paper 84-0006*, January 1984.
- [4] Zhong, X., "Leading-Edge Receptivity to Free Stream Disturbance Waves for Hypersonic Flow Over A Parabola," *Journal of Fluid Mechanics*, Vol. 441, 2001, pp. 315-367.
- [5] Herbert, T. and Esfahanian, V., "Stability of Hypersonic Flow over a Blunt Body," *AGARD CP-514*, Vol. pp. 28-1 - 12, April, 1993.
- [6] Esfahanian, V., *Computation and stability analysis of laminar flow over a blunt cone in hypersonic flow*, Ph.D. thesis, The Ohio State University, 1991.
- [7] Fedorov, A. V. and Khokhlov, A. P., "Prehistory of Instability in a Hypersonic Boundary Layer," *Theoretical and Computational Fluid Dynamics*, Vol. 14, 2001, pp. 359-375.

- [8] Kendall, J. M., "Wind Tunnel Experiments Relating to Supersonic and Hypersonic Boundary-Layer Transition," *AIAA Journal*, Vol. 13, No. 3, pp. 290-299, 1975.
- [9] Malik, M. R., Lin, R. S., and Sengupta, R., "Computation of Hypersonic Boundary-Layer Response to External Disturbances," *AIAA Paper 99-0411*, January 1999.
- [10] Ma, Y. and Zhong, X., "Receptivity to Freestream Disturbances of Mach 4.5 Flow over A Flat Plate," *AIAA Paper 2002-0140*, January 2002.
- [11] Whang, C. W. and Zhong, X., "Receptivity of Gortler Vortices in Hypersonic Boundary Layers," *AIAA Paper 2002-0151*, January 2002.
- [12] Tumin, A. and Reshotko, E., "Spatial Theory of Optimal Disturbances in Boundary Layers," *Physics of Fluids*, Vol. 13, No. 7, July 2001.
- [13] Carpenter, M. H., Gotlieb, D., and Abarbanel, S., "The Stability of Numerical Boundary Treatments for Compact High-Order Finite-Difference Schemes," *Journal of Computational Physics*, Vol. 108, 1993, pp. 272-295.
- [14] Zhong, X. and Tatineni, M., "Stable High-Order Schemes and DNS of Boundary-Layer Stability on a Blunt Cone at Mach 8," *AIAA Paper 2001-0437*, 2001.
- [15] Malik, M. R., Spall, R. E., and Chang, C.-L., "Effect of Nose Bluntness on Boundary Layer Stability and Transition," *AIAA paper 90-0112*, 1990.
- [16] Kufner, E., Dallmann, U., and Stilla, J., "Instability of Hypersonic Flow Past Blunt Cones - Effects of Mean Flow Variations," *AIAA paper 93-2983*, June 1993.
- [17] Kufner, E. and Dallmann, U., "Entropy- and Boundary Layer Instability of Hypersonic Cone Flows - Effects of Mean Flow Variations," *IUTAM Symposium on Laminar-Turbulent Transition*, Vol. Sendai/Japan, September 1994, pp. 197-204, Springer-Verlag, Berlin, 1994.
- [18] Malik, M. R., "Numerical Methods for Hypersonic Boundary Layer Stability," *Journal of Comp. Phys.*, Vol. 86, 1990, pp. 376-413.
- [19] Mack, L. M., "Boundary Layer Linear Stability Theory," *AGARD report, No. 709*, 1984, pp. 3-1 to 3-81.

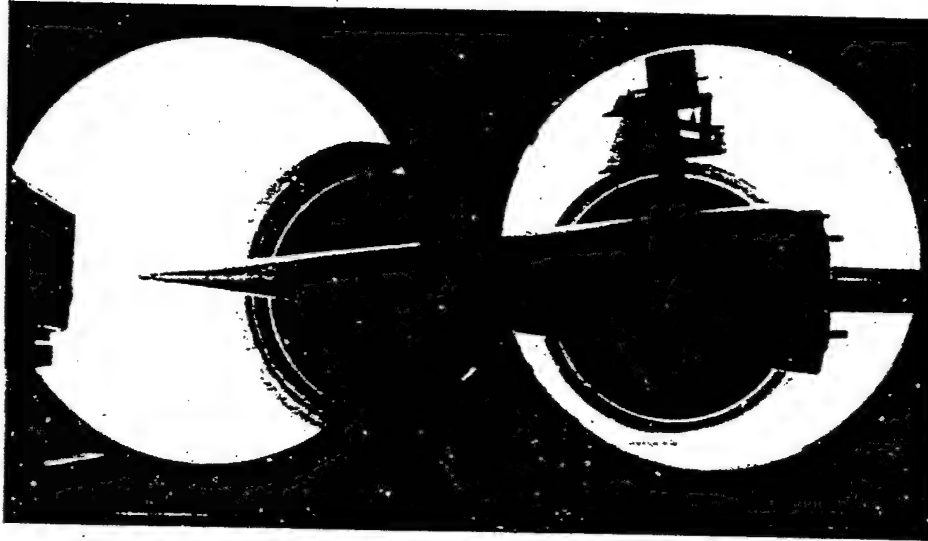


Figure 1: The 7° half-angle blunt cone of Stetson et al.'s (1984) Mach 7.99 stability experiment.

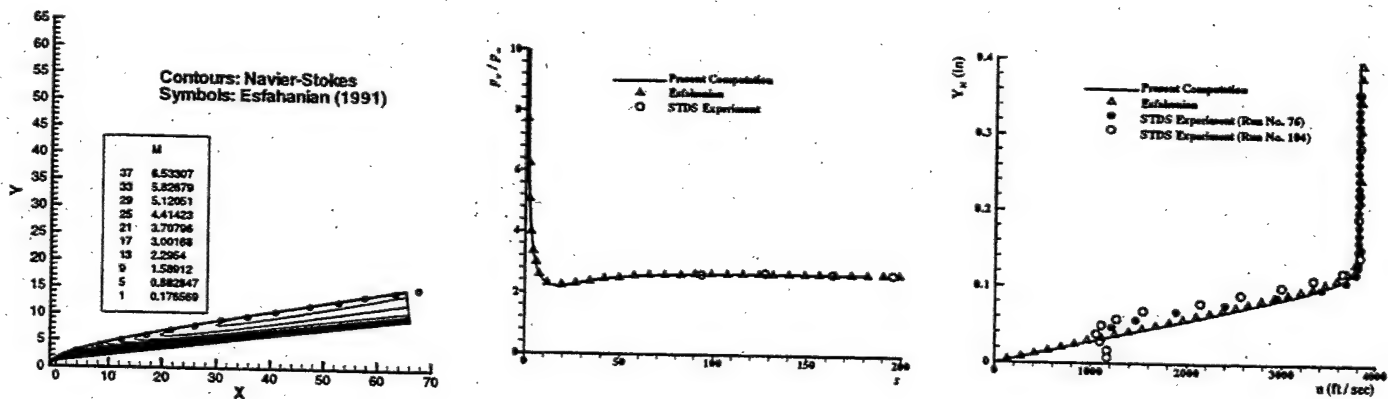


Figure 2: Steady flow solution for Mach 7.99 flow over a 7° half-angle blunt cone with an adiabatic wall: Mach number contours, pressure along the cone surface, and tangential velocity profiles at 128 nose radii surface location.

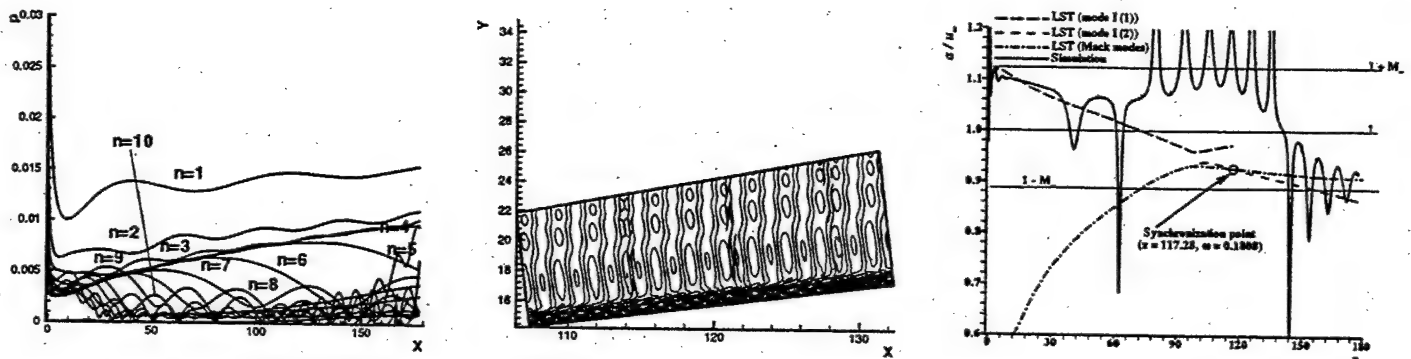


Figure 3: Results of receptivity simulation: 1) pressure perturbations along the cone surface; 2) contours of temperature perturbations ($f^* = 149.2 \text{ kHz}$, $n = 10$); 3) phase velocities along the cone surface at frequencies of $n = 10$.

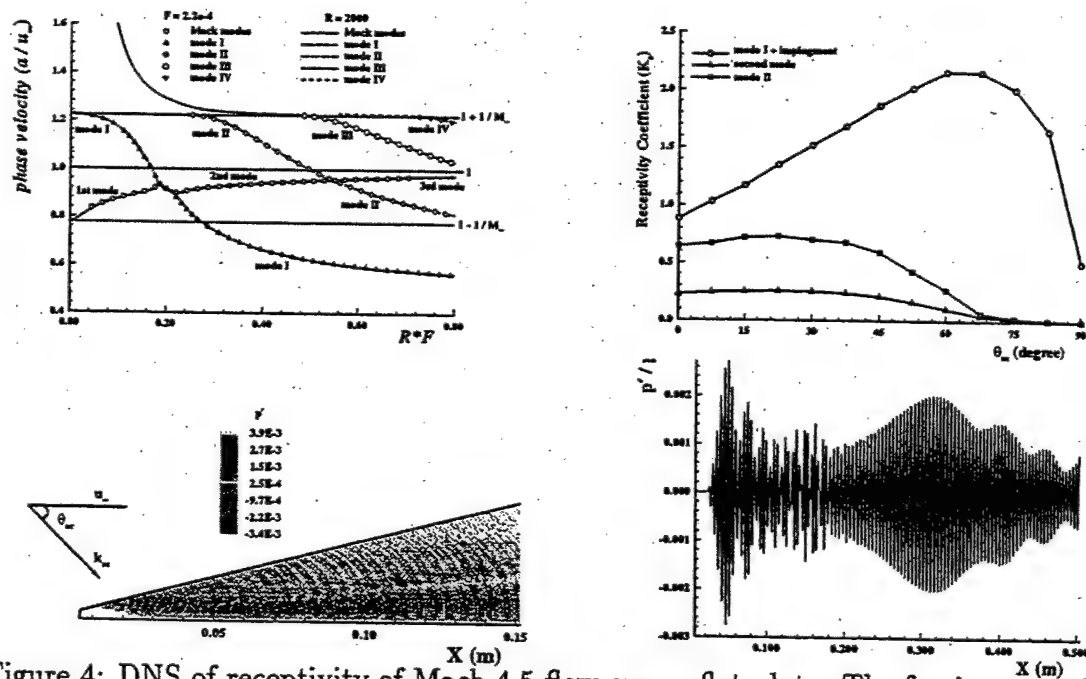


Figure 4: DNS of receptivity of Mach 4.5 flow over a flat plate. The forcing wave is a plane acoustic wave with zero angle ($F = 2.2 \times 10^{-4}$).

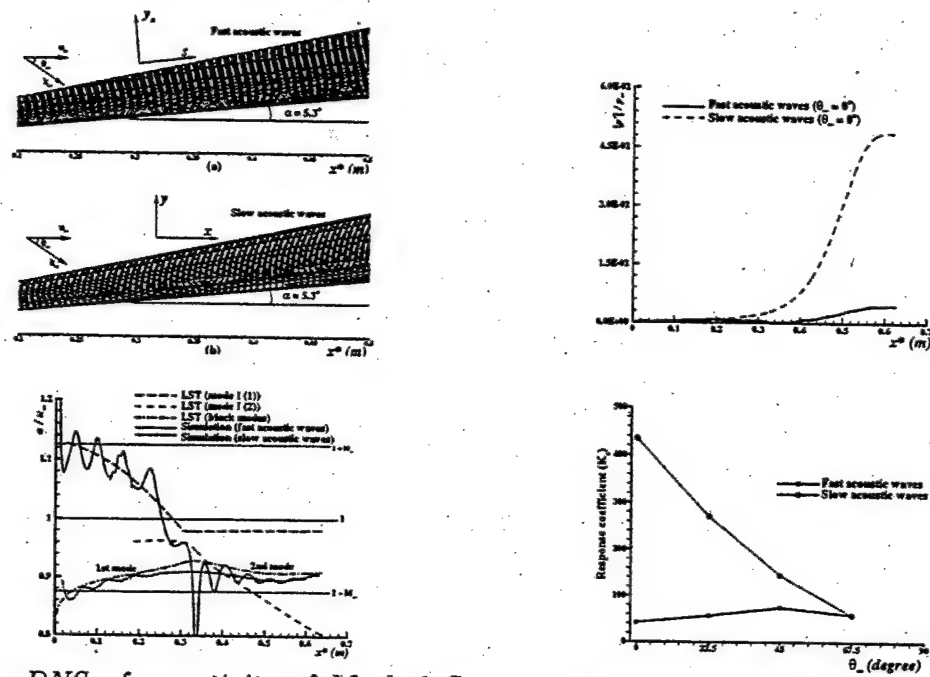


Figure 5: DNS of receptivity of Mach 8 flow over a sharp wedge. The forcing waves are plane fast and slow acoustic wave with zero angle at 100kHz: 1) instantaneous pressure perturbation contours; 2) distribution of phase velocities; 3) response coefficients of the second mode; 4) pressure perturbations along the wall surface.

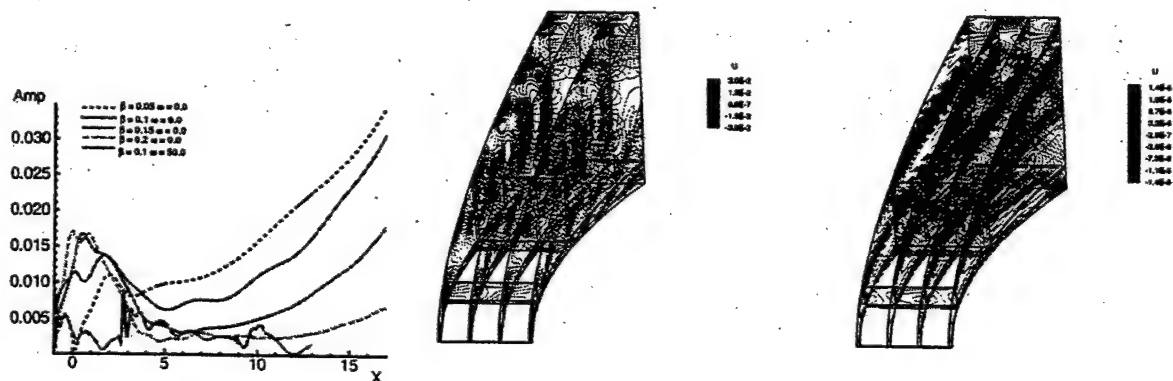
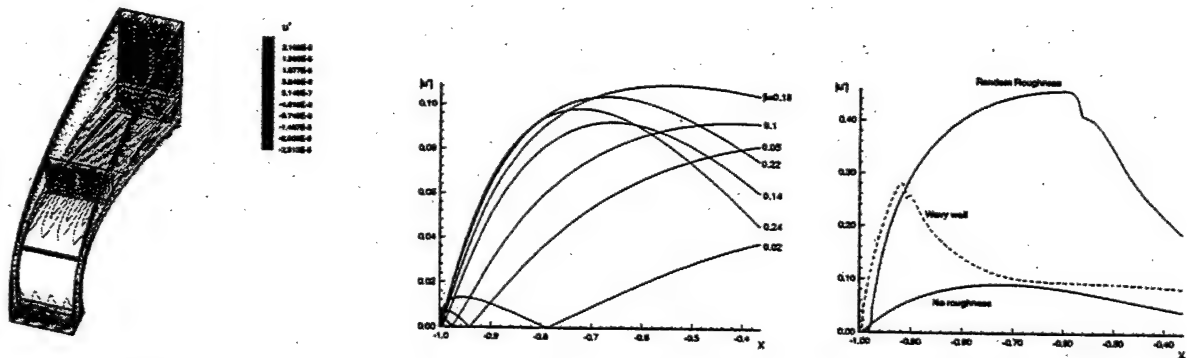
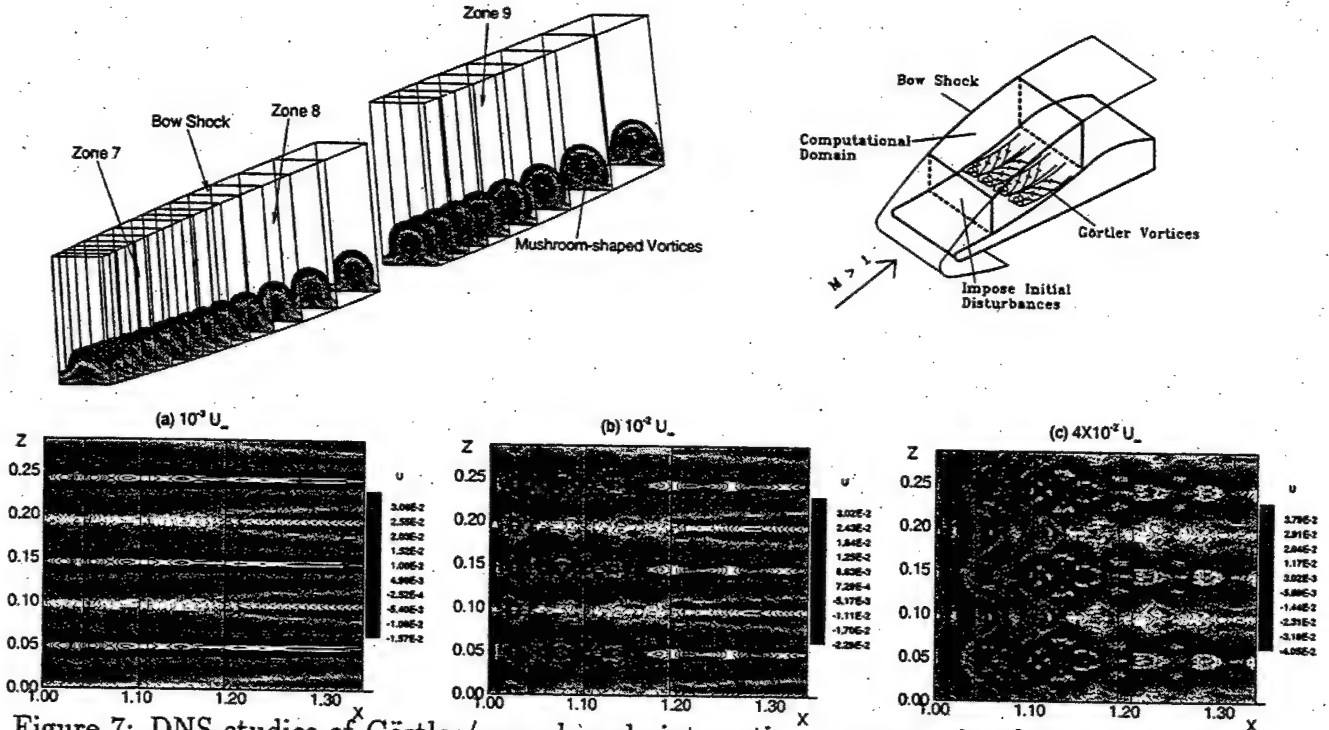


Figure 6: DNS of receptivity of Görtler vortices in a Mach 15 flow over a blunt wedge induced by freestream vorticity wave: disturbance amplitude distributions, and streamwise velocity disturbance contours at $\omega = 50$ and 0.



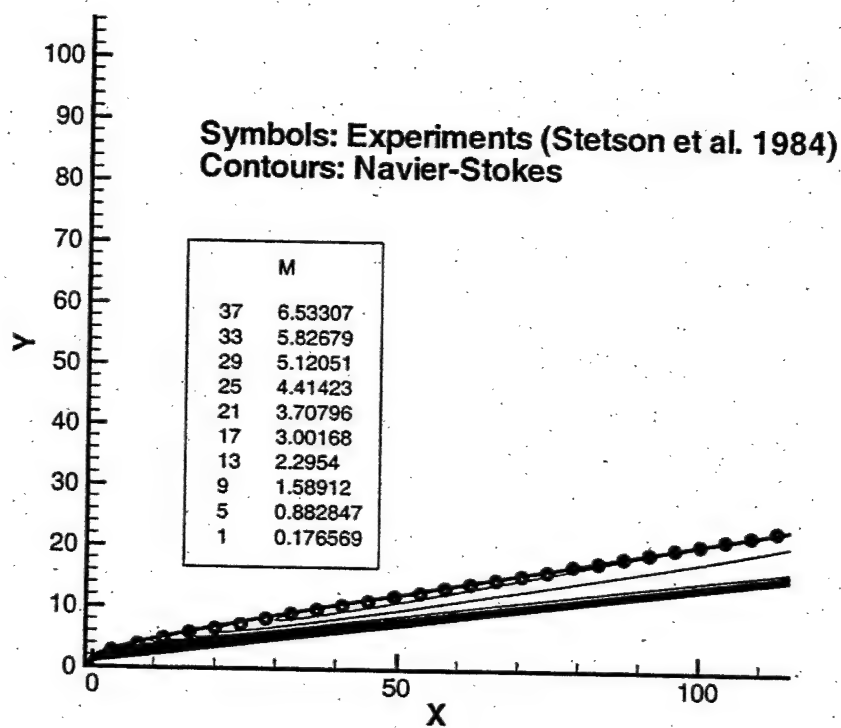


Figure 9: Mach number contours for steady Mach 7.99 flow over a 7° half-angle blunt cone. The experimental bow shock shape (Stetson et al., 1984) is compared with the current numerical solutions.

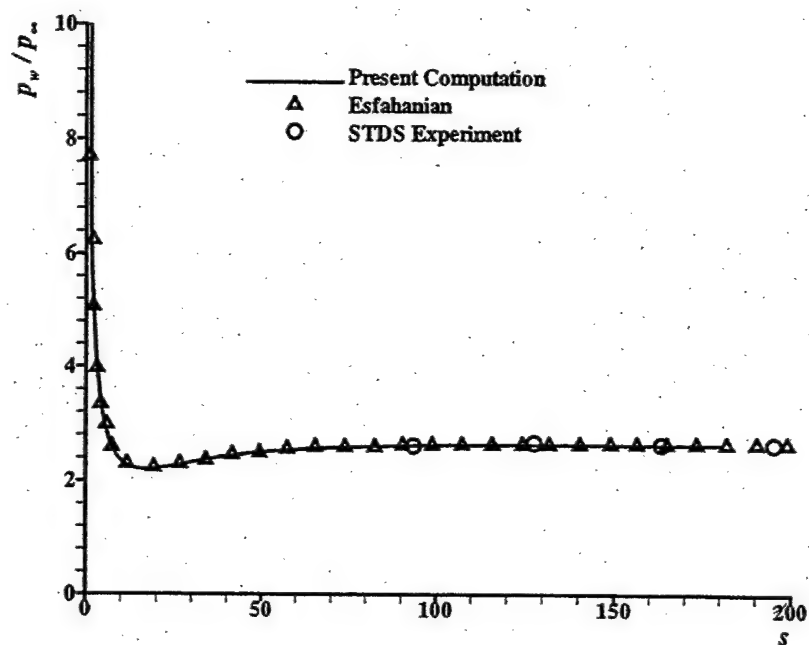


Figure 10: Steady pressure along the cone surface.

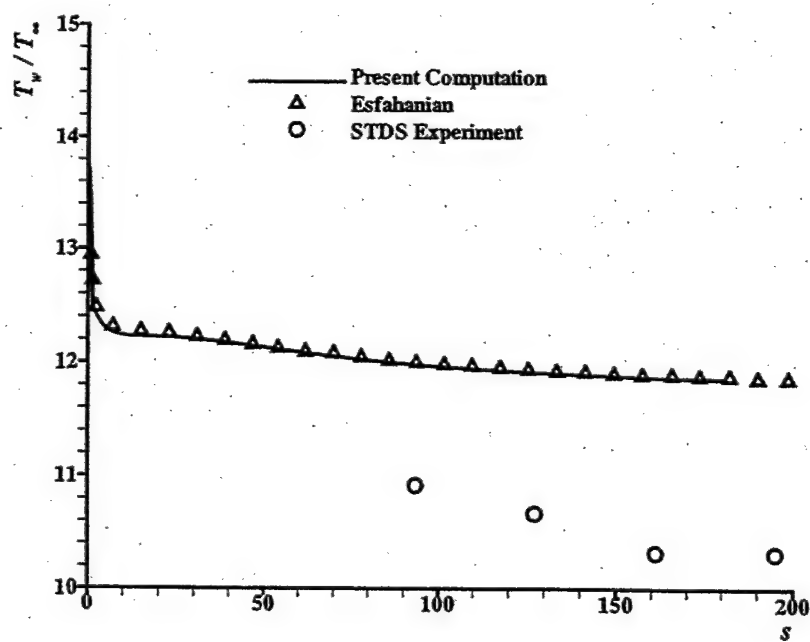


Figure 11: Steady temperature along the cone surface.

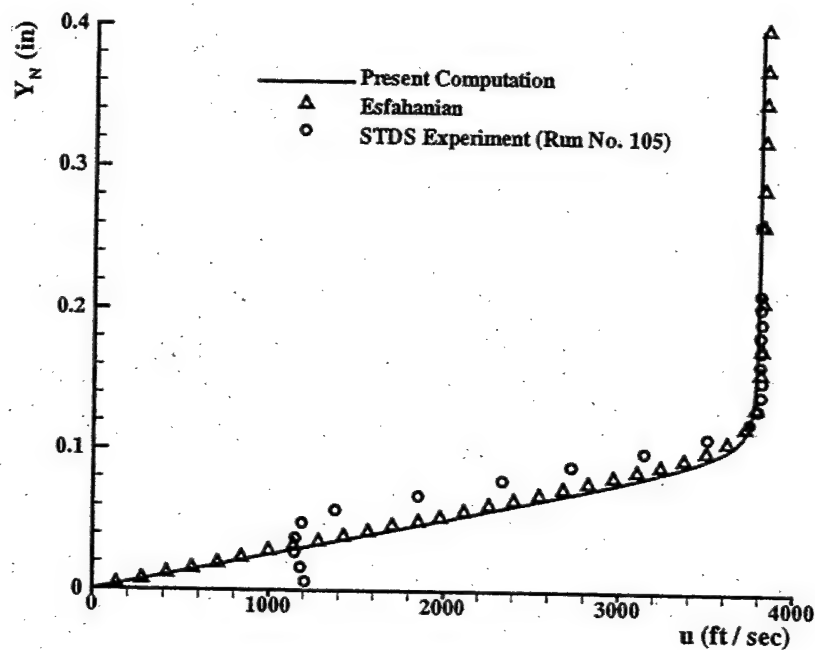


Figure 12: Steady tangential velocity profiles along the wall-normal direction at the surface location of 94 nose radii.

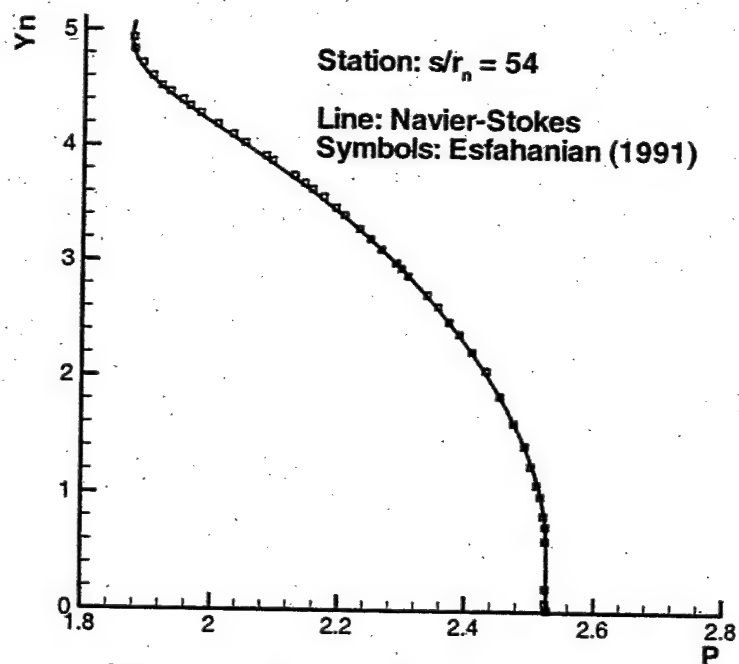


Figure 13: Pressure profiles at station $s = 54$. The results are compared with those of Esfahanian and Herbert (1991).

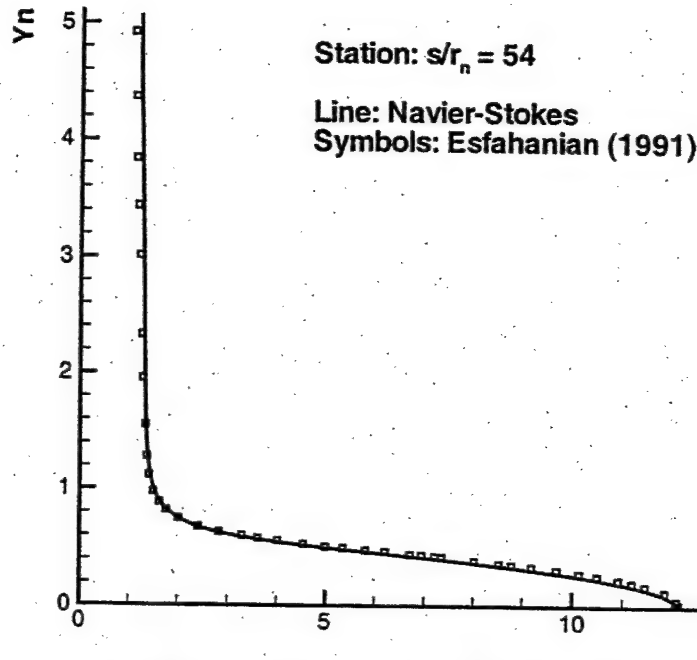


Figure 14: Temperature profiles at station $s = 54$. The results are compared with those of Esfahanian and Herbert (1991).

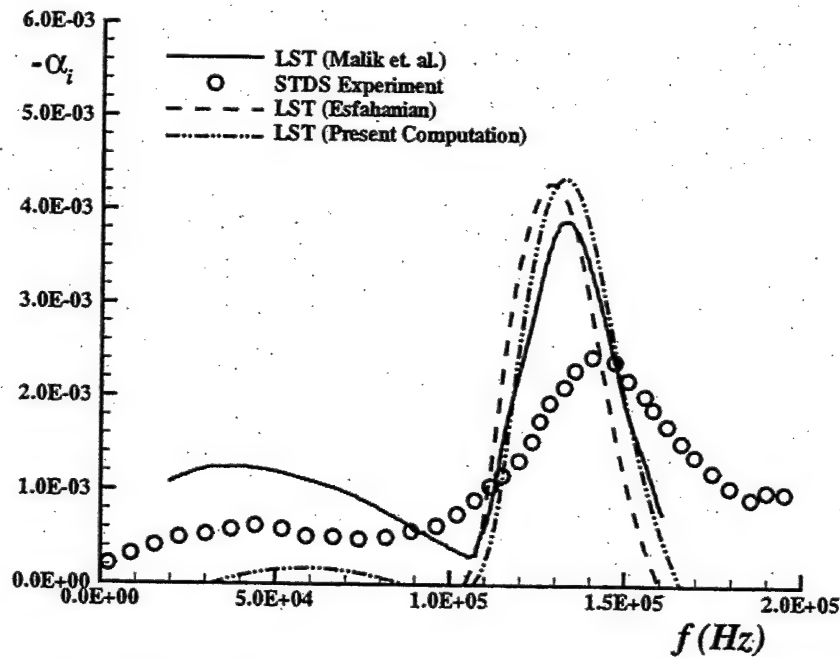


Figure 15: Comparison of disturbance growth rates predicted by LST and experiments at $s = 175$ ($x = 172$).

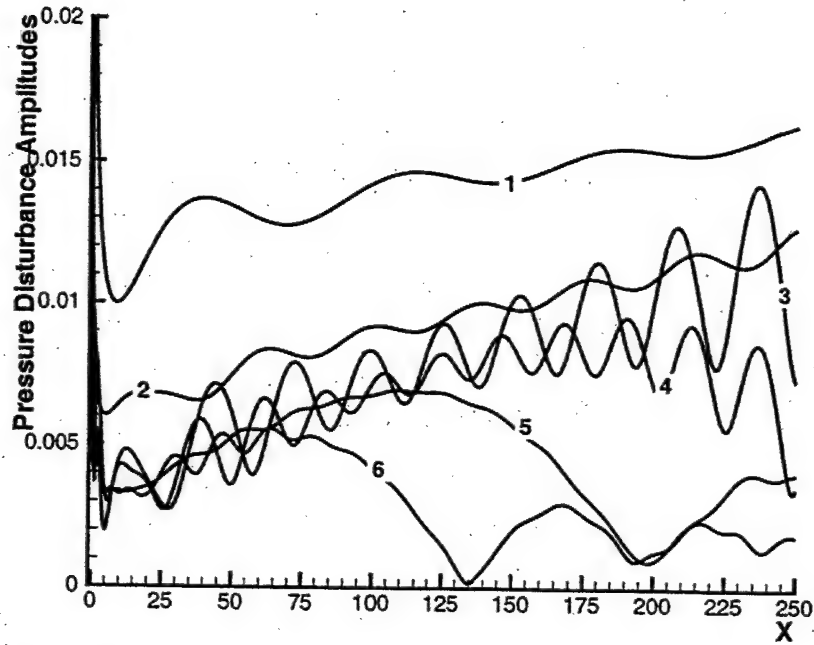


Figure 16: Amplitudes of pressure perturbations on the cone surface vs. x . The lines represent 6 different frequencies of $f_n = n f_1$, where $f_1^* = 14.922 kHz$ and $n = 1, 2, \dots, 6$.

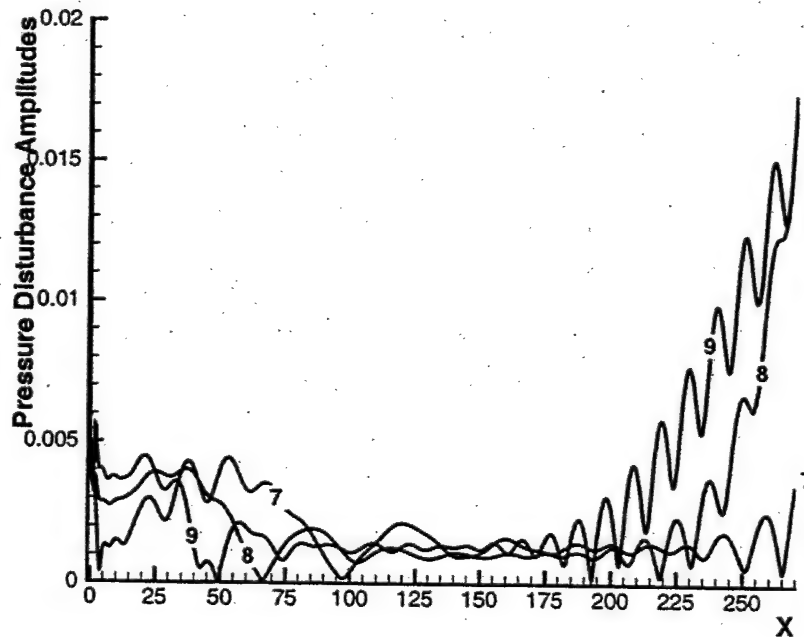


Figure 17: Amplitudes of pressure perturbations on the cone surface vs. x . The lines represent 3 different frequencies of $n = 7, 8, 9$.

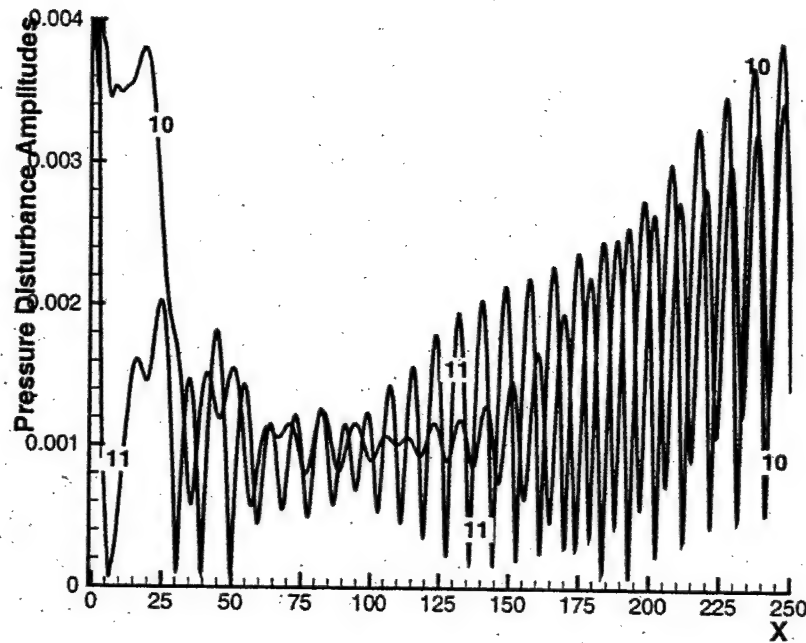


Figure 18: Amplitudes of pressure perturbations on the cone surface vs. x . The lines represent 2 different frequencies of $n = 10, 11$.

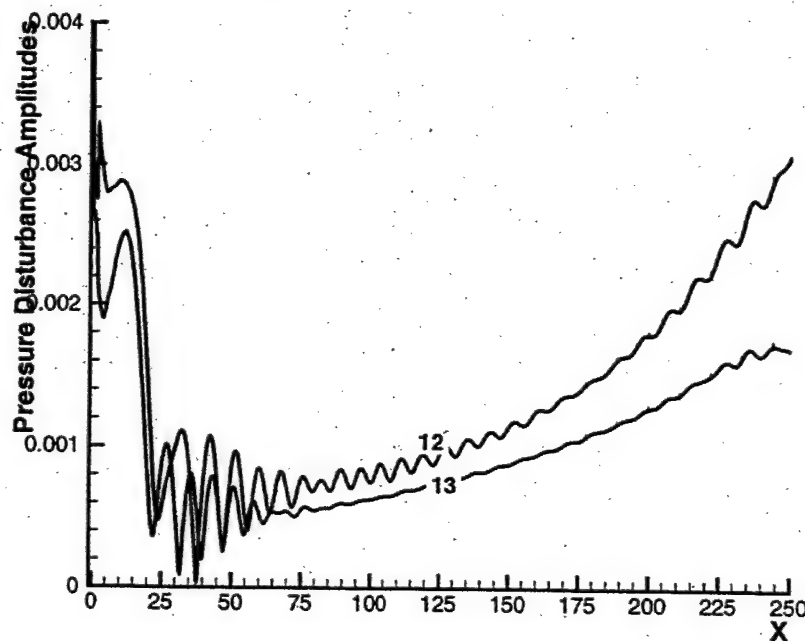


Figure 19: Amplitudes of pressure perturbations on the cone surface vs. x . The lines represent 2 different frequencies of $n = 12, 13$.

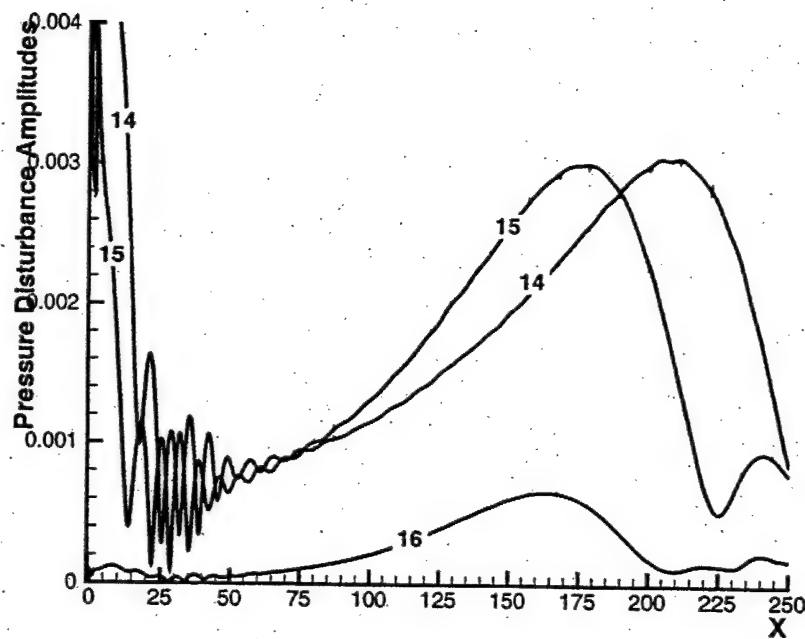


Figure 20: Amplitudes of pressure perturbations on the cone surface vs. x . The lines represent 3 different frequencies of $n = 14, 15, 16$.

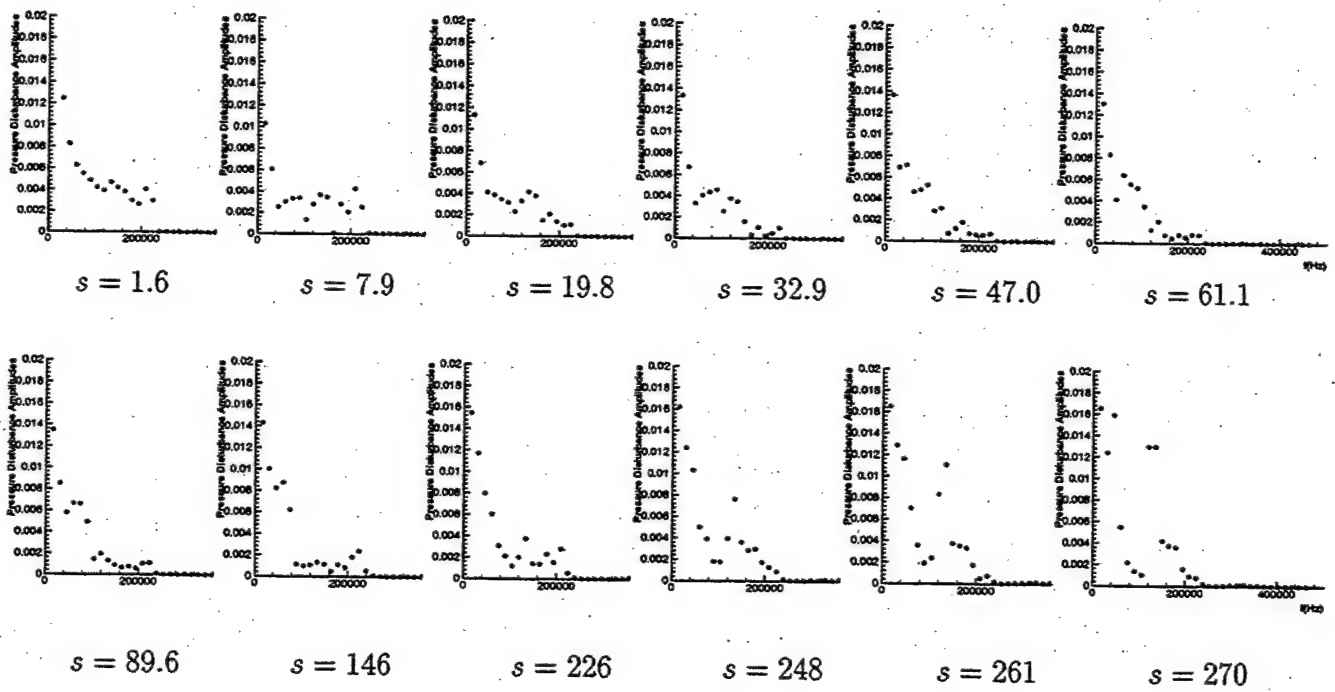
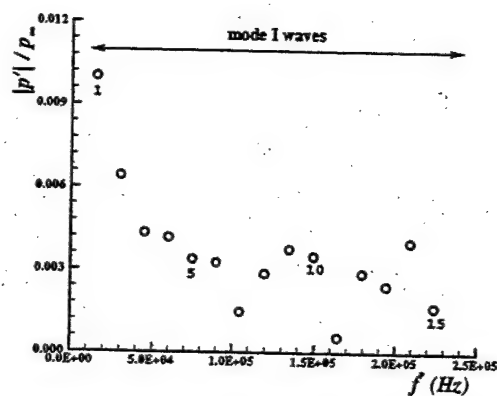
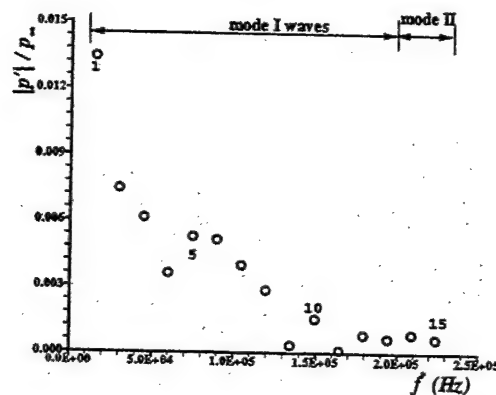


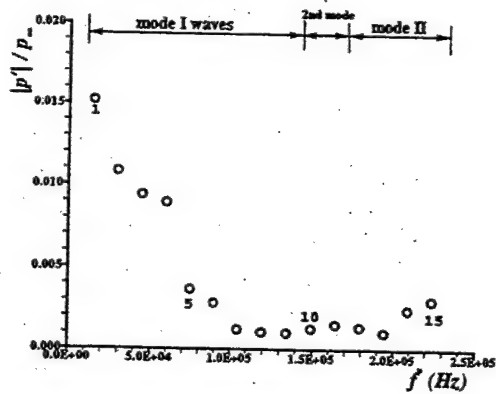
Figure 21: The frequency spectrum of the pressure perturbations on the cone surface at a number of surface locations.



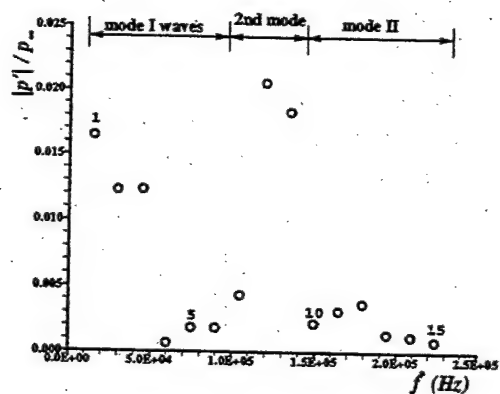
$s = 11$



$s = 52$



$s = 174$



$s = 274$

Figure 22: The frequency spectrum of the pressure perturbations on the cone surface at a number of surface locations.

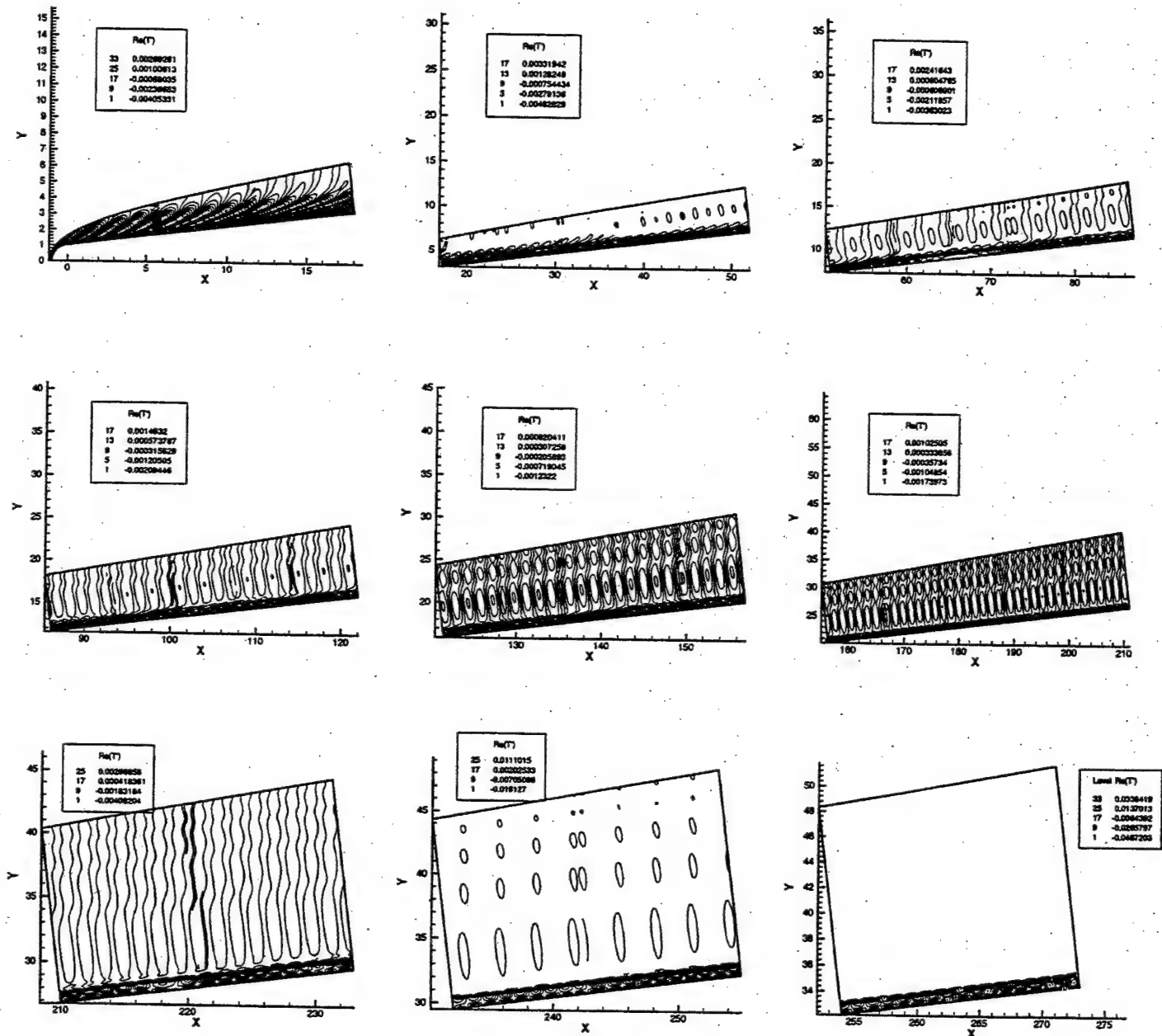


Figure 23: Contours of real part of temperature perturbations in the flow field for the frequency of $f^* = 119.4kHz$ ($n = 8$).

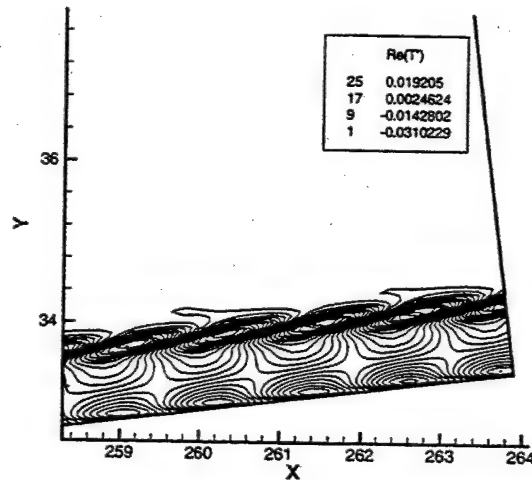
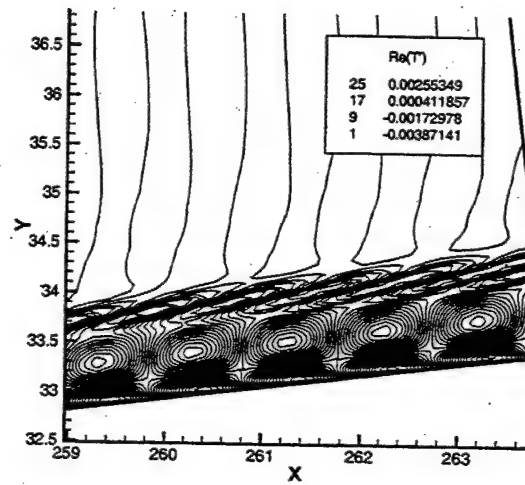
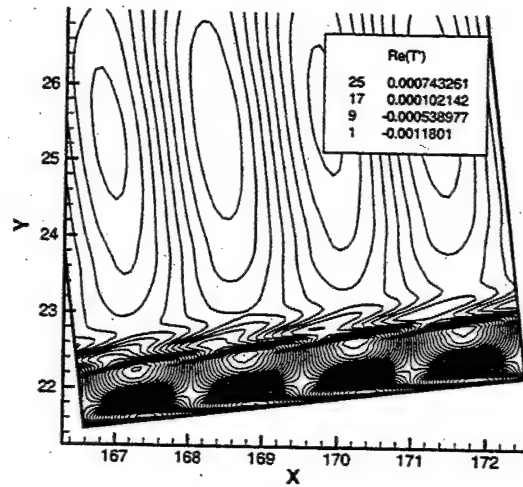


Figure 24: Contours of real part of temperature perturbations in a localized region of the flow field for three different modes: top figure, mode I at $f^* = 119.4 \text{ kHz}$ ($n = 8$); mid figure, mode II at $f^* = 179.1 \text{ kHz}$ ($n = 12$); bottom figure, second Mack mode at $f^* = 119.4 \text{ kHz}$ ($n = 8$).

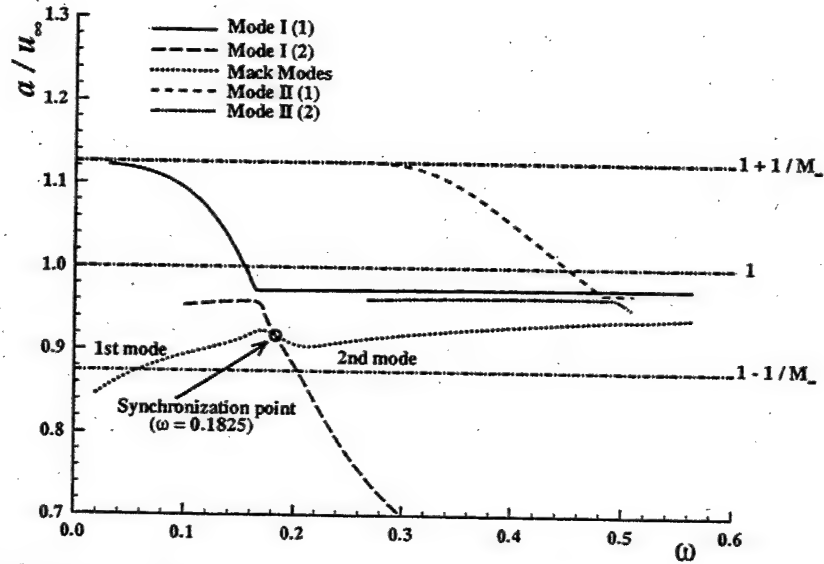


Figure 25: Phase velocities of three discrete modes, i.e., mode I, mode II and the Mack modes, changing with frequencies at the station $s = 175$.

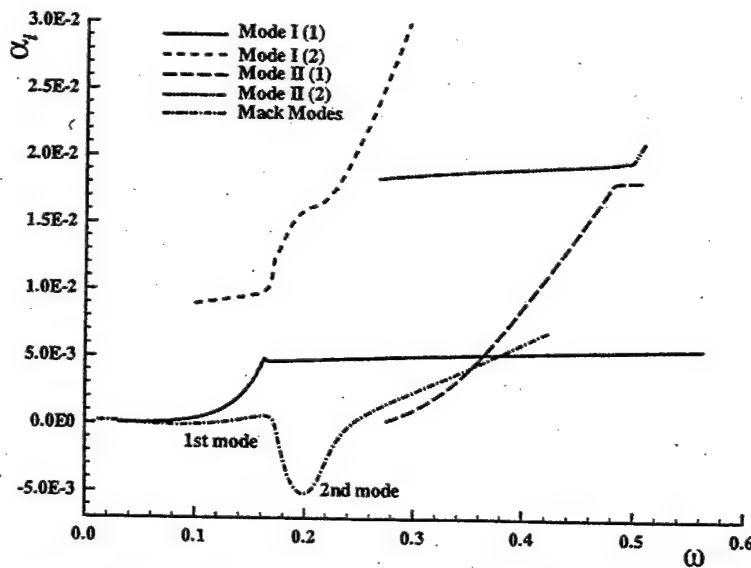


Figure 26: Growth rates of three discrete modes, i.e., mode I, mode II and the Mack modes, changing with frequencies at the station $s = 175$.

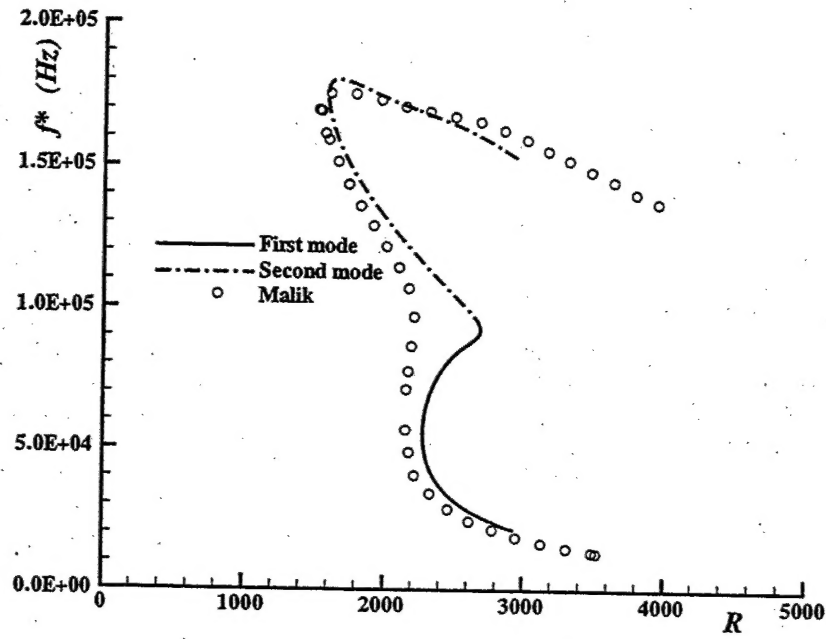


Figure 27: Comparison of the neutral curve of Mack modes with Malik's (1990) results.

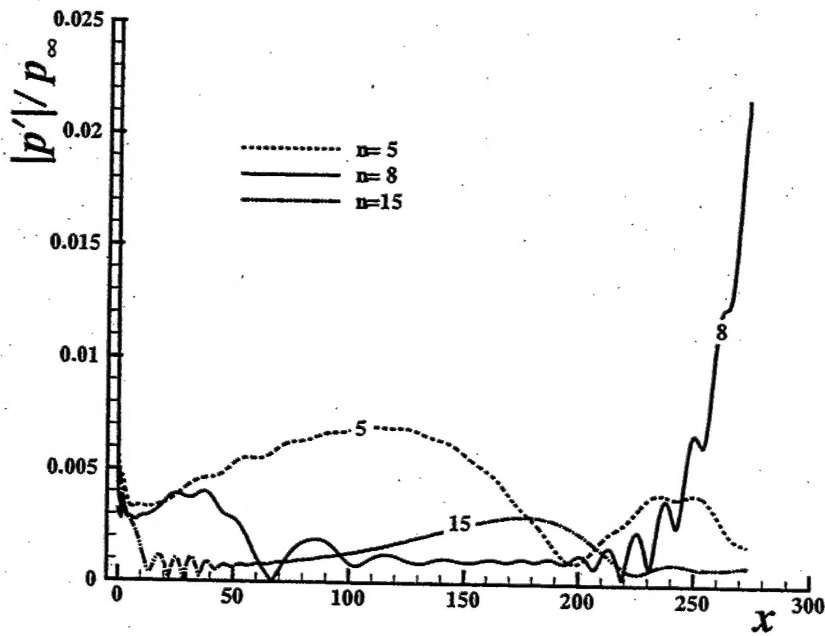


Figure 28: The evolution of pressure perturbations on the wall due to freestream disturbances at three frequencies.

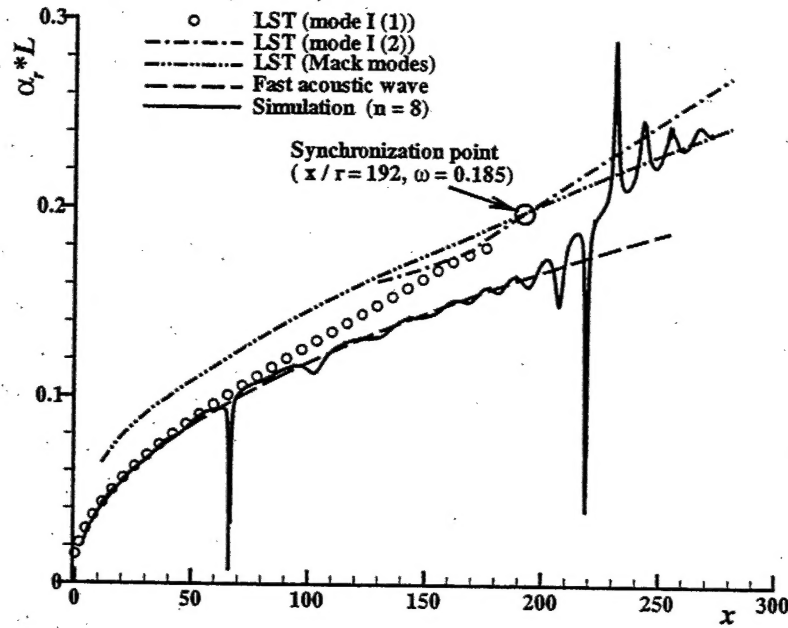


Figure 29: The distribution of the streamwise wave number of induced boundary-layer disturbances at frequency with $n = 8$ ($f^* = 119.4 kHz$) from the simulation.

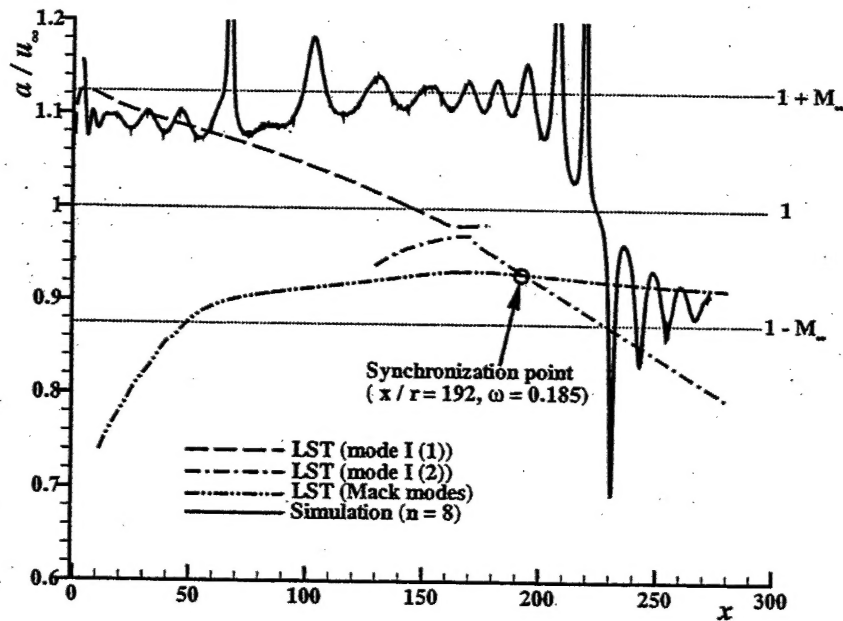


Figure 30: Comparison of phase velocity of induced boundary-layer disturbances at frequency with $n = 8$ ($f^* = 119.4 kHz$) from the simulation with that of boundary-layer normal modes from the LST.

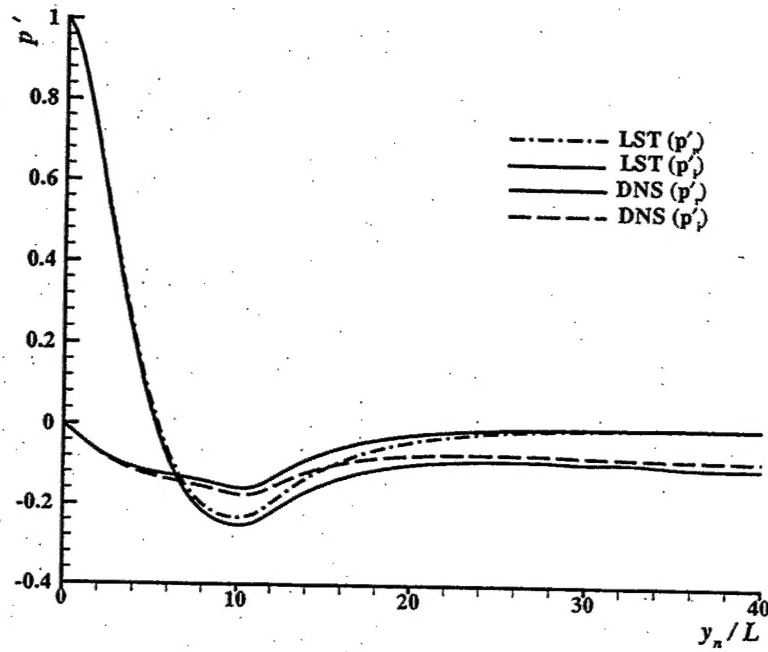


Figure 31: Profiles of induced disturbances in the numerical simulation at $x = 271$ compared with the second Mack mode waves from the LST ($n = 8$).

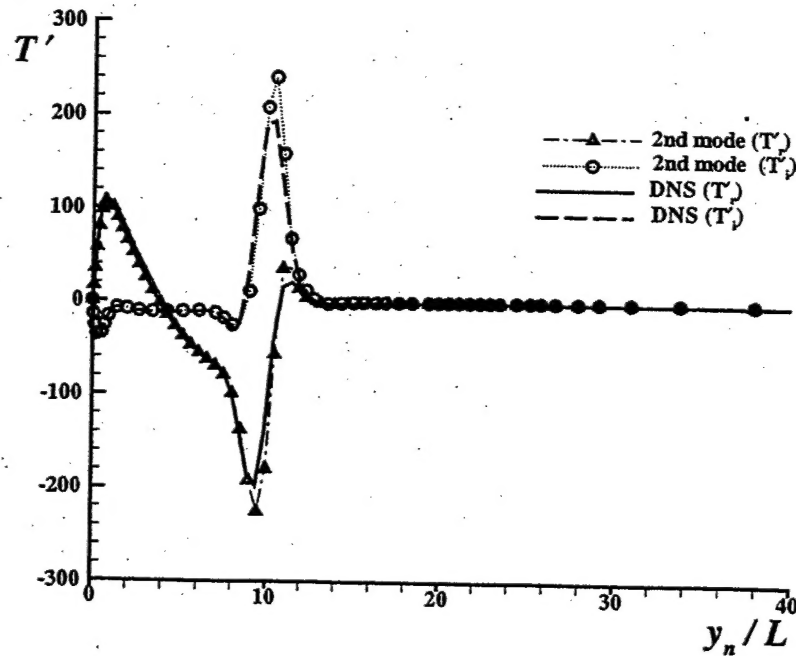


Figure 32: Profiles of induced disturbances in the numerical simulation at $x = 271$ compared with the second Mack mode waves from the LST ($n = 8$).

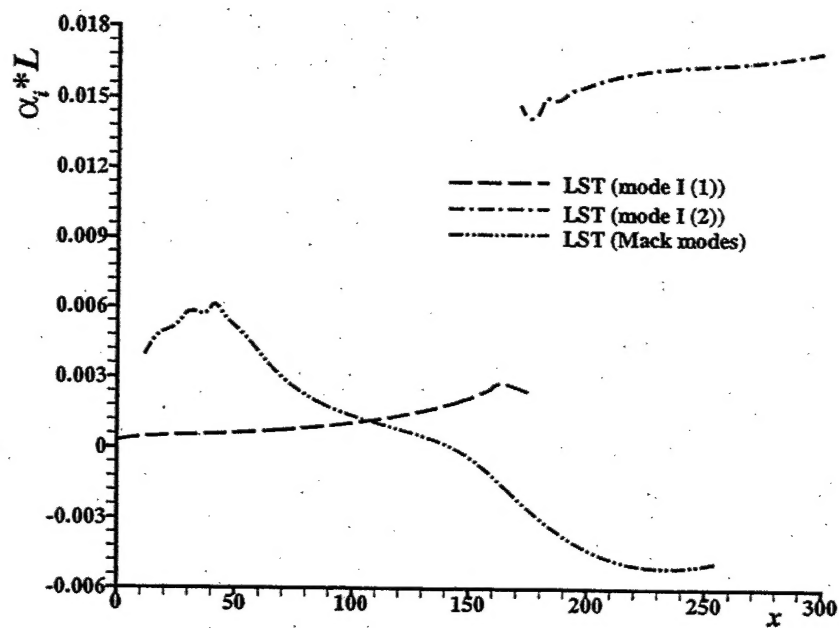


Figure 33: Distribution of growth rates of boundary-layer normal modes at frequency with $n = 8$.